Available online at www.sciencedirect.com

ScienceDirect

Geochimica et Cosmochimica Acta 189 (2016) 70–95

Geochimica et Cosmochimica Acta

www.elsevier.com/locate/gca

A link between oxygen, calcium and titanium isotopes in ^{26}Al-poor hibonite-rich CAIs from Murchison and implications for the heterogeneity of dust reservoirs in the solar nebula

Levke Kööp [a,b,c,*], Andrew M. Davis [a,b,c,d], Daisuke Nakashima [e,f], Changkun Park [g,h], Alexander N. Krot [g], Kazuhide Nagashima [g], Travis J. Tenner [e], Philipp R. Heck [a,b,c], Noriko T. Kita [e]

[a] *Department of the Geophysical Sciences, The University of Chicago, Chicago, IL, USA*
[b] *Chicago Center for Cosmochemistry, The University of Chicago, Chicago, IL, USA*
[c] *Robert A. Pritzker Center for Meteoritics and Polar Studies, Field Museum of Natural History, Chicago, IL, USA*
[d] *Enrico Fermi Institute, The University of Chicago, Chicago, IL, USA*
[e] *Dept. Geoscience, University of Wisconsin-Madison, WI, USA*
[f] *Division of Earth and Planetary Materials Science, Tohoku University, Sendai, Japan*
[g] *HIGP/SOEST University of Hawai'i at Mānoa, Honolulu, HI, USA*
[h] *Korea Polar Research Institute, Incheon, Republic of Korea*

Received 30 July 2015; accepted in revised form 6 May 2016; Available online 13 May 2016

Abstract

PLACs (platy hibonite crystals) and related hibonite-rich calcium-, aluminum-rich inclusions (CAIs; hereafter collectively referred to as PLAC-like CAIs) have the largest nucleosynthetic isotope anomalies of all materials believed to have formed in the solar system. Most PLAC-like CAIs have low inferred initial ^{26}Al/^{27}Al ratios and could have formed prior to injection or widespread distribution of ^{26}Al in the solar nebula. In this study, we report ^{26}Al–^{26}Mg systematics combined with oxygen, calcium, and titanium isotopic compositions for a large number of newly separated PLAC-like CAIs from the Murchison CM2 chondrite (32 CAIs studied for oxygen, 26 of these also for ^{26}Al–^{26}Mg, calcium and titanium). Our results confirm (1) the large range of nucleosynthetic anomalies in ^{50}Ti and ^{48}Ca (our data range from −70‰ to +170‰ and −60‰ to +80‰, respectively), (2) the substantial range of Δ^{17}O values (−28‰ to −17‰, with $\Delta^{17}O = \delta^{17}O - 0.52 \times \delta^{18}O$), and (3) general ^{26}Al-depletion in PLAC-like CAIs.

The multielement approach reveals a relationship between Δ^{17}O and the degree of variability in ^{50}Ti and ^{48}Ca: PLAC-like CAIs with the highest Δ^{17}O (∼−17‰) show large positive and negative ^{50}Ti and ^{48}Ca anomalies, while those with the lowest Δ^{17}O (∼−28‰) have small to no anomalies in ^{50}Ti and ^{48}Ca. These observations could suggest a physical link between anomalous ^{48}Ca and ^{50}Ti carriers and an ^{16}O-poor reservoir. We suggest that the solar nebula was isotopically heterogeneous shortly after collapse of the protosolar molecular cloud, and that the primordial dust reservoir, in which anomalous carrier phases were heterogeneously distributed, was ^{16}O-poor ($\Delta^{17}O \geqslant -17‰$) relative to the primordial gaseous ($CO + H_2O$)

* Corresponding author at: Department of the Geophysical Sciences, The University of Chicago, Chicago, IL, USA.
E-mail address: koeoep@uchicago.edu (L. Kööp).

http://dx.doi.org/10.1016/j.gca.2016.05.014

reservoir ($\Delta^{17}O < -35‰$). However, other models such as CO self-shielding in the protoplanetary disk are also considered to explain the link between oxygen and calcium and titanium isotopes in PLAC-like CAIs.

Keywords: Platy hibonite crystals (PLACs); CAI; Meteorites; Solar nebula; Oxygen isotopes; Titanium isotopes; Calcium isotopes; Aluminum-26

1. INTRODUCTION

Oxygen is unique among the chemical elements in the solar system in that significant fractions were present in solid and gaseous states over a large range of temperatures in the solar nebula. Meteoritic materials show mass-independent variations in oxygen isotopes that are of extraordinary magnitude for a major rock-forming element. For example, many calcium-, aluminum-rich inclusions (CAIs), the oldest dated materials that formed in the solar system (e.g., Connelly et al., 2012), are enriched in ^{16}O by ~5% compared to terrestrial planets and asteroids (Clayton et al., 1973; MacPherson et al., 2008; Makide et al., 2009; Ushikubo et al., 2011). The degree of enrichment/depletion in ^{16}O is commonly expressed using the $\Delta^{17}O$ value, ($\Delta^{17}O = \delta^{17}O - 0.52 \times \delta^{18}O$, with δ-values being defined as $\delta^{i}O = [(^{i}O/^{16}O)_{unknown}/(^{i}O/^{16}O)_{VSMOW} - 1] \times 1000$, for isotope i and where VSMOW corresponds to Vienna standard mean ocean water; Baertschi, 1976), which allows for comparison of ^{16}O-enrichment even for materials with mass-dependent isotope fractionation in oxygen. Analyses of solar wind collected by NASA's Genesis mission confirmed a prediction (Clayton, 2002) that the Sun, like most CAIs, is enriched in ^{16}O relative to the Earth and terrestrial planets (McKeegan et al., 2011). As the Sun contains most of the mass of the solar system and is thus representative of its average composition, it is not CAIs but terrestrial planets that are highly aberrant in their oxygen isotopic composition. Several models have been proposed to explain this discrepancy, which are either based on inheritance of distinct nucleosynthetic oxygen isotope reservoirs from the molecular cloud core (Krot et al., 2010) or isotopically selective gas phase reactions. The latter include self-shielding during photodissociation of CO molecules followed by water ice/CO gas fractionation and thermal processing of silicate dust in a gaseous reservoir enriched in ^{17}O and ^{18}O (Clayton, 2002; Yurimoto and Kuramoto, 2004; Lyons and Young, 2005), as well as symmetry-based reactions (Thiemens, 2006).

Many CAIs seem to have formed in a uniform oxygen isotopic reservoir that was slightly depleted in ^{16}O compared to the solar $\Delta^{17}O$ value of $-28.4 \pm 3.6‰$ ($\pm 2\sigma$; McKeegan et al., 2011). For example, CAIs from CR chondrites and the primitive ungrouped chondrite Acfer 094 commonly show a $\Delta^{17}O$ value of approximately −23‰ (Makide et al., 2009; Ushikubo et al., 2011). Many CV CAIs likely formed in a similar reservoir, as indicated by the common $\Delta^{17}O$ value of ~−23‰ in spinel, hibonite, fassaite (Al, Ti-diopside), and forsterite grains (e.g., MacPherson et al., 2008). More ^{16}O-poor compositions in melilite and anorthite in the same CV CAIs are commonly interpreted as subsequent mineral-dependent exchange with or remelting in a ^{16}O-poor reservoir (Krot et al., 2009, and references therein). However, $\Delta^{17}O$ variations in some CV and CO CAIs have also been attributed to fluctuations in the isotopic composition of the CAI formation region (e.g., Simon et al., 2011; Kawasaki et al., 2012; Park et al., 2012). Additional important exceptions from the uniform CAI value are several grossite-rich CAIs and a chondrule from CH carbonaceous chondrites that are ^{16}O-enriched relative to the Sun's value ($\Delta^{17}O$ as low as −37‰; Kobayashi et al., 2003; Krot et al., 2008, 2015; Gounelle et al., 2009).

In addition to oxygen isotopes, CAIs provide important information about the presence of various nucleosynthetic components in the solar nebula. For example, most CV CAIs incorporated the short-lived (half-life of ~0.7 Ma) radionuclide ^{26}Al at a uniform $^{26}Al/^{27}Al$ ratio of $\sim 5.2 \times 10^{-5}$, called the canonical ratio (Jacobsen et al., 2008; MacPherson et al., 2012). In addition, CAIs show small-scale anomalies in stable isotopes like ^{50}Ti, ^{96}Zr, and ^{92}Mo, typically within ~1‰ of the terrestrial values (e.g., Schönbächler et al., 2003; Trinquier et al., 2009; Burkhardt et al., 2011; Akram et al., 2013). In the context of this study, we define "regular CAIs" as those having (1) a uniform $\Delta^{17}O$ of about −23‰, (2) a canonical $^{26}Al/^{27}Al$ ratio, and (3) small-scale nucleosynthetic anomalies.

When compared to regular CAIs, FUN (fractionated and unidentified nuclear effects) CAIs and PLACs (platy hibonite crystals) are isotopically distinct. In particular, both FUN CAIs and PLACs have lower inferred $^{26}Al/^{27}Al$ ratios than regular CAIs, and some have evidence for formation in the absence of ^{26}Al (e.g., Wasserburg et al., 1977; Ireland, 1990; Liu et al., 2009; Park et al., 2013). This ^{26}Al deficiency is commonly attributed to an early formation prior to arrival of ^{26}Al rather than a late formation after ^{26}Al decay, because FUN CAIs and PLACs preserve larger nucleosynthetic anomalies than regular CAIs (Wood, 1998; Sahijpal and Goswami, 1998). In PLACs, nucleosynthetic anomalies can be up to two orders of magnitude greater than in CV CAIs (e.g., PLACs have a $\delta^{50}Ti$ range of ~300‰; Hinton et al., 1987; Ireland, 1990; Liu et al., 2009); in FUN CAIs, the range of anomalies is intermediate between PLACs and regular CV CAIs (e.g., FUN CAIs have a $\delta^{50}Ti$ range of ~35‰; Krot et al., 2014; Park et al., 2014). The $\Delta^{17}O$ values of these ^{26}Al-poor, anomalous CAIs also span a wide range from ~−28‰ to ~0‰ (Liu et al., 2009; Krot et al., 2008, 2010, 2014, 2015), indicating oxygen isotopic heterogeneity in the earliest stages of solar system history.

PLACs may be uniquely suited to constrain the origin of the solar system's early variation in oxygen isotopes. Their large nucleosynthetic anomalies indicate that they could be among the first objects that formed inside the solar system. In addition, and in contrast to FUN CAIs, their isotopic signatures have not been overprinted by high degrees of mass-dependent fractionation (Ireland, 1990; Liu et al., 2009). While the oxygen isotopic compositions of FUN CAIs are generally consistent with pre-evaporation compositions close to the carbonaceous chondrite anhydrous mineral (CCAM; Clayton et al., 1977) line (Mendybaev et al., 2013), the exact position of their precursors relative to the line remains unclear. A recent study found that the oxygen isotopic compositions of PLACs fall along the CCAM line like regular CAIs and chondrules (Liu et al., 2009), suggesting that a single process could have been responsible for the oxygen isotope variations in the early solar system.

Based on their potential as a robust recorder of the isotopic evolution of the early solar system, we present precise oxygen isotopic compositions obtained with high spatial resolution for a large number of newly recovered, carefully prepared PLACs from the Murchison CM2 chondrite. In addition, we analyzed many of these CAIs for magnesium, calcium, and titanium isotopes to better characterize their formation environment and the relationships between different isotopic components in the early solar system. The results show a clear relationship between the oxygen isotopic composition and the magnitude of anomalies in calcium and titanium isotopes, which may be indicative of the processes responsible for oxygen isotopic variation in the early solar system. In addition, we confirm the differences between the titanium isotopic patterns in PLACs and in other solar system materials and use our calcium and titanium isotopic patterns to investigate the stellar sources that contributed material to the early solar system.

2. METHODS

2.1. Sample recovery and selection

Many of the hibonite-rich CAIs were separated from a 92 g piece of the Murchison meteorite from the Field Museum meteorite collection (FMNH ME 2644). This was achieved by disaggregation with dental tools, which included removal of the fusion crust, followed by repeated freezing and thawing while immersed in high purity water (Fisher Optima™ grade). The hibonite-rich CAIs were concentrated by density separation using an organic heavy liquid (Cargille Labs, density 3.31 g cm^{-3}). The heavy fraction was then washed in high purity acetone and isopropanol (both Fisher Optima™ grade) and distributed among 25 dishes, from which CAI candidates were picked. Additional hibonite-rich objects were recovered from an existing Murchison acid-residue (Amari et al., 1994). The samples were mounted on conductive carbon tape and their mineral chemistry was confirmed by energy-dispersive X-ray spectroscopy (EDS). The focus of this study is on the refractory, ^{26}Al-poor and isotopically anomalous types of hibonite-rich CAIs. Other hibonite-bearing objects, such as SHIBs and highly mass-fractionated hibonites, were obtained in the same process and were isotopically and chemically analyzed in the same sessions (Kööp et al., 2015, 2016).

2.2. Sample preparation

After removal from the conductive tape, the hibonite-rich CAIs were cleaned with high purity isopropanol (Fisher Optima™ grade) and dried. Together with terrestrial mineral standards, the hibonite-rich CAIs were mounted in one-inch diameter epoxy disks. During polishing with a combination of lapping films and polishing pads, care was taken to prepare flat surfaces to avoid instrumental mass fractionation due to topography (Kita et al., 2009). The polishing relief was checked using a Zygo profilometer at the University of Wisconsin and was found to be minimal in nine randomly selected mounts. Specifically, height differences between grains and epoxy were $\leqslant$2 μm, and the typical profile over a one-inch disk surface was $\leqslant$10 μm. The polished mounts were carbon-coated for chemical and isotopic analyses.

2.3. Electron microscopy

The hibonite-rich CAIs were characterized using scanning electron microscopy (SEM) with a Zeiss EVO 60 at the Field Museum and a JEOL JSM-5800LV at the University of Chicago, both equipped with Oxford Instruments EDS systems. Backscattered electron (BSE) images, secondary electron images, and EDS analyses were collected on both unpolished and polished samples for petrologic characterization and for identifying the most suitable locations for isotope analysis.

2.4. Electron microprobe analysis

Quantitative chemical analyses were performed with a CAMECA SX-50 electron probe microanalyzer (EPMA) at the University of Chicago. Most of the samples were analyzed with a 100 nA beam and an acceleration voltage of 20 kV; only the inclusions with small grain sizes were analyzed with a 50 nA beam and a 15 kV acceleration voltage. Mineral standards were manganese hortonolite for magnesium and iron, corundum for aluminum, and anorthite for calcium. We observed negative magnesium contents on the corundum standard due to curvature in the background caused by the intense aluminum peak, therefore, we corrected for the curvature using data obtained from multiple peak scans of a magnesium-free corundum standard. The effect of this correction is negligible for all CAIs presented here.

2.5. Isotopic analyses

2.5.1. Oxygen

Oxygen isotope analyses were performed with the WiscSIMS CAMECA IMS 1280 (Kita et al., 2009, 2010) using a protocol similar to that of Nakashima et al. (2011). A small primary Cs^+ beam (~20 pA, ~3 × 4 $μm^2$) was chosen, primarily to preserve material for further isotopic analysis and to avoid sampling of adjacent

minerals or alteration phases. Simultaneous detection of the three oxygen isotopes was achieved using a Faraday cup (FC) for $^{16}O^-$ and electron multipliers (EM) for $^{17}O^-$ and $^{18}O^-$. San Carlos olivine was used as a running standard and a WiscSIMS hibonite standard was used for instrumental bias correction. Two to four spot analyses were collected in each CAI, and nine to thirteen unknown analyses were bracketed by eight analyses of the San Carlos olivine standard. The external reproducibility of the running standard (~1‰ (2 standard deviation (SD)) for $\delta^{18}O$, $\delta^{17}O$, and $\Delta^{17}O$) was assigned as the analytical uncertainty of unknown samples (see Kita et al., 2009). The contribution of the tailing of $^{16}OH^-$ interference to $^{17}O^-$ signal was corrected using the method of Heck et al. (2010), though the contribution was negligibly small (≤0.5‰). After oxygen isotope analysis, the SIMS pits were checked with the SEM to verify that only primary, single phases had been sampled. Analyses from questionable pits (i.e., pits that were found to contain epoxy or other primary or secondary phases) were rejected. Oxygen was the first element studied by SIMS in all CAIs to avoid problems with ion implantation from the primary $^{16}O^-$ beam, which was used for magnesium, calcium, and titanium isotopic measurements. Analyses of oxygen isotope standards are presented in Table EA.1.

2.5.2. Aluminum–magnesium

Magnesium isotopes in hibonite were analyzed with the WiscSIMS CAMECA IMS-1280 using monocollection EM detection combined with an additional multicollector FC detector for simultaneous detection of ^{27}Al (Kita et al., 2012; Ushikubo et al., 2013). The measurements were performed in two separate sessions, both of which used a ~9 μm diameter primary O^- beam. The primary beam intensity was 0.15 nA, secondary $^{24}Mg^+$ signals were within a range of (0.3–1.7) × 10^5 cps. The Madagascar hibonite (MH) standard was analyzed to determine relative sensitivity factors (RSF) between $^{27}Al^+$ and $^{24}Mg^+$ signals, as was done in previous studies (Ireland, 1988; Liu et al., 2012). The $^{24}Mg^+$ signal of the hibonite standard was at the high end of the acceptable EM range (4 × 10^5 cps), which would result in a dead time correction inaccuracy of ~1‰. Therefore, we used an anorthite glass standard with MgO contents comparable to unknown hibonites (1 wt%; Kita et al., 2012) to estimate the instrumental bias correction for excess ^{26}Mg ($\delta^{26}Mg^*$), in order to avoid any potential inaccuracy of EM dead time brought about by analyzing the hibonite standard with a much higher Mg^+ secondary ion intensity. We also used anorthite to correct for instrumental mass fractionation in $\delta^{25}Mg$, which could have introduced a systematic bias due to the matrix effect between anorthite and hibonite. However, a comparison of anorthite and Madagascar hibonite standard measurements shows that this effect is small. Counting times of individual ions for each cycle were 3 s for $^{24}Mg^+$ and 10 s for $^{25}Mg^+$, $^{26}Mg^+$, and $^{27}Al^+$, respectively; the total number of cycles for each magnesium isotope analysis was between 20 and 40, with resulting uncertainties of 2.9‰ and 2.5‰ on $\delta^{26}Mg^*$, 1.5‰ and 1.4‰ on both $\delta^{25}Mg$ and $\delta^{26}Mg$. As the primary objective was to evaluate whether the studied CAIs belong to the ^{26}Al-poor population or not, we sometimes chose to acquire fewer cycles (i.e., 20 instead of 40) to maximize the number of analyzed unknowns.

Excess ^{26}Mg was calculated using the relationship $\delta^{26}Mg^* = \delta^{26}Mg - [(1 + \delta^{25}Mg/1000)^{1/\beta} - 1] \times 1000$ (Kita et al., 2012; Davis et al., 2015). We used the updated β value of 0.5128 (Davis et al., 2015), however, no difference outside of quoted uncertainties is observed when the previously recommended β value of 0.514 (Davis et al., 2005) is applied. As most analyzed CAIs are single hibonite crystals, initial $^{26}Al/^{27}Al$ ratios can only be inferred from model isochrons by assuming an initial magnesium isotopic composition (the common assumption is that $\delta^{26}Mg^*_0 = 0‰$). However, this assumption is only relevant for a limited number of samples, as most unknowns do not show excess ^{26}Mg, despite high $^{27}Al/^{24}Mg$ ratios. Analyses of magnesium isotope standards are presented in Table EA.1.

2.5.3. Calcium and titanium

The calcium and titanium isotopic compositions were measured with a CAMECA IMS-1280 at the University of Hawai'i at Mānoa in 26 of the hibonite-rich CAIs that had been studied for oxygen isotopes. The analytical protocol used was similar to that of Park et al. (2014), which is based on previous studies of hibonite-rich CAIs (Fahey et al., 1987a,b; Ireland, 1990). A primary $^{16}O^-$ beam with a current of 0.4–0.6 nA and a diameter of 15–18 μm was used for both MH standards and unknowns. ^{40}Ca ((1.5–4) × 10^6 cps) was detected by FC; all other isotopes of calcium and titanium as well as $^{51}V^+$, $^{52}Cr^+$, $^{53}Cr^+$ and $^{87}Sr^{2+}$ were measured sequentially using the monocollection EM detector (count-rates for calcium and titanium isotopes were between 2 × 10^3 and <1 × 10^5 cps on EM). 60 cycles were acquired with counting times of 2 s for ^{40}Ca, ^{44}Ca, and ^{48}Ti, 4 s for ^{42}Ca, 4.96 s for ^{46}Ti, ^{47}Ti, ^{48}Ca, ^{49}Ti, ^{50}Ti, ^{51}V, ^{52}Cr, and ^{53}Cr, 10 s for ^{43}Ca, and 0.96 s for $^{87}Sr^{2+}$, resulting in a total of ~1.5 h for each analysis. The relative detection efficiency of the FC relative to the EM was determined from calcium isotopic measurements on standards assuming that $\Delta^{40}Ca$ plots on a linear mass fractionation line defined by $\Delta^{42}Ca$, $\Delta^{43}Ca$, and $\Delta^{48}Ca$ (Δ-values are defined as $\Delta^{i}Ca = [(^{i}Ca/^{44}Ca)_{measured}/(^{i}Ca/^{44}Ca)_{terrestrial} - 1] \times 1000$); the calculated FC yield using 22 standard measurements is 1.011 ± 0.025 (2 standard errors, SE). An EM dead time of 28.9 ± 2.1 ns (2 SE) was determined from titanium isotopic measurements on a TiO_2 standard and was corrected using methods similar to Fahey et al. (1987a) and Fahey (1998); the effect of the uncertainty in the dead time measurement is negligibly small for the CAIs studied. The magnification of the transfer optics was ~160. Contrast and field aperture sizes of 400 and 3000 μm, respectively, were chosen to transmit most secondary ions but to avoid transmission of scattered ions and ions with large emitted angles. The entrance and exit slits were set to 31 and 94 μm, respectively, which resulted in a mass resolving power (MRP) of ~11,170 defined at 10% of peak height. Compared to fully opened entrance slits and field aperture, the resulting transmission was ~11%. The MRP was similar to that of Liu et al. (2009) and was chosen to resolve ^{48}Ca from ^{48}Ti. With this

MRP, the tail of the ^{48}Ti peak at the center of the ^{48}Ca peak had decreased by a factor of $\sim 4 \times 10^{-5}$, which corresponds to a contribution of the ^{48}Ti tail to ^{48}Ca of less than ~1.5‰ in this study and is thus not resolvable within 2σ uncertainties. A few isobaric interferences on other masses cannot be resolved at this MRP and required correction. Interference of ^{46}Ca on ^{46}Ti was corrected by assuming a terrestrial ^{46}Ca/^{44}Ca ratio for unknowns. ^{52}Cr and ^{51}V were monitored during analysis for possible interference of ^{50}Cr and ^{50}V on ^{50}Ti. While contributions are mostly insignificant

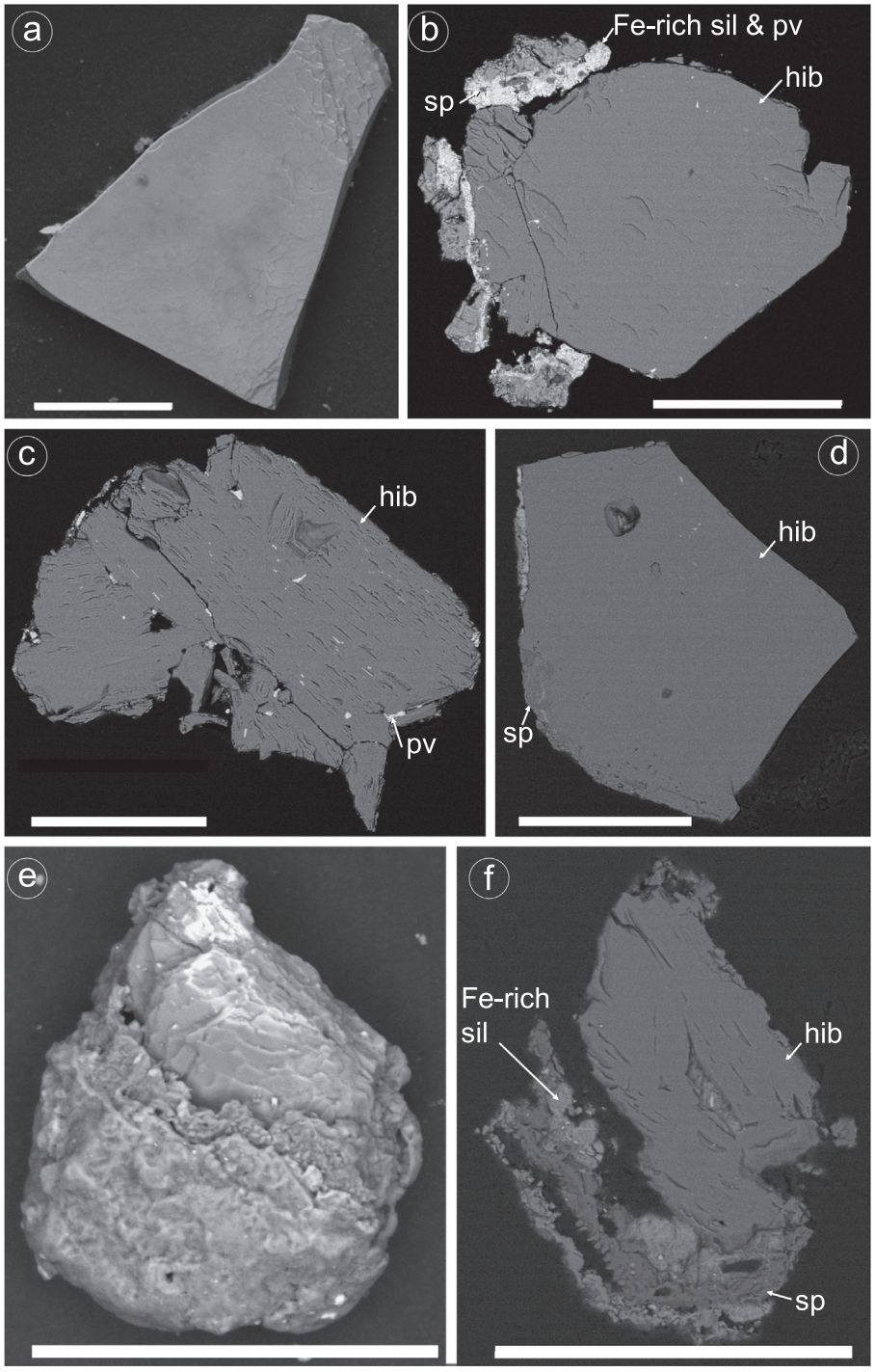

Fig. 1. BSE images of unpolished and polished hibonite-rich CAIs with scale bars corresponding to 50 μm. (a) Platy hibonite crystal, unpolished. (b) Stubby hibonite crystal, partially surrounded by a silicate rim containing small crystals of perovskite and spinel. (c) Polished hibonite aggregate with perovskite inclusions. (d) Hibonite plate with spinel margin (dark gray, left). (e, f) Hibonite aggregate (2-6-9) before (e) and after polishing (f). The aggregate is partially surrounded by a rim of alteration phases (FeO-rich silicates), spinel and a calcium- and magnesium-rich silicate (possibly diopside).

($\leqslant$0.3‰ for ^{50}Cr and ^{50}V; exception is CAI 2-7-3, with a ^{50}Cr correction of 0.8‰ to the δ^{50}Ti value), corrections were applied that assume terrestrial isotopic abundances. While the assumption of terrestrial isotopic abundances might be considered problematic for PLAC hibonites, no significant bias is expected for ^{50}Ti as Cr and V abundances are low (variations in excess of 1000‰ would be required for ^{50}Cr/^{52}Cr and ^{50}V/^{51}V to affect δ^{50}Ti values outside of uncertainty). Similarly, large anomalies in excess of ~100‰ would be required for ^{46}Ca/^{44}Ca to cause a bias on δ^{46}Ti outside of quoted uncertainties. In contrast to previous studies, we chose to correct for instrumental fractionation by sample-standard bracketing and propagated uncertainties of MH standard measurements, because the exponential law commonly used in previous studies may not be appropriate to correct instrumental mass fractionation accurately (Park et al., 2014; see Appendix A.3). A Rayleigh law was used to correct for intrinsic mass fractionation of calcium and titanium isotopes, assuming that possible evaporation of calcium and titanium occurred in the form of calcium atoms and TiO_2 molecules, respectively, as recommended by Zhang et al. (2014). The uncertainties were propagated from unknown (2 SE of 60 cycles) and standard analyses (2 SD of bracket average). For calcium, the normalization pair was ^{40}Ca and ^{44}Ca. For titanium, we consider both ^{49}Ti/^{47}Ti and ^{46}Ti/^{48}Ti normalization. Due to the relatively large beam size, cavities, some of which contained epoxy and/or alteration phases, could not be avoided in a few hibonite aggregates. However, post-SIMS EDS analyses of such alteration phases showed that these are iron- and magnesium-rich silicates with no significant calcium and titanium abundances. Therefore, dilution of nucleosynthetic effects due to contamination should be minimal for all samples.

3. RESULTS

3.1. Petrologic characteristics

The 32 samples included in this study are mostly sizeable hibonite-rich CAIs (30 to 150 μm) that were deemed suitable for study of multiple isotopic systems. Many of these CAIs ($N = 14$) are single hibonite crystals that have a range of morphologies from platy (Fig. 1a) to stubby to equant (Fig. 1b). Additional samples include spinel-free polycrystalline hibonite aggregates ($N = 8$; Fig. 1c) and a small number of hibonite crystals and aggregates with spinel margins or spinel rims ($N = 4$; Fig. 1d–f). In addition, there are six hibonite-rich CAIs with irregular shapes that could be either single crystals or aggregates. Perovskite is a common phase both at grain boundaries in hibonite aggregates and as inclusions inside hibonite crystals, where it often forms thin layers along cleavage planes of hibonite (Fig. 1c). Iron oxide-rich alteration phases are sometimes preserved in non-acid-treated samples, filling voids in aggregates and forming layers within the rims of some samples (Fig. 1e–f).

Hibonite grains in most of the CAIs or CAI fragments are magnesium-poor (0.1 to 0.2 Mg atoms per formula unit, pfu), with the exception of two spinel-free hibonite aggregates (1-3-2 and 2-6-3) with magnesium contents up to 0.4 Mg pfu (Table 1). Titanium abundances generally correlate with magnesium, consistent with a coupled substitution of Mg^{2+} and Ti^{4+} for two Al^{3+}; however, slight excesses in titanium could hint at an additional presence of Ti^{3+} (Table 1). FeO is only above the detection limit (0.08 wt% for 20 kV and 0.03 wt% at 15 kV analyses) in four hibonite aggregates. While iron may be contamination in the case of the extremely fine-grained aggregate 1-3-2 and aggregate 1-5-3, which has abundant alteration phases between hibonite crystals, aggregates 1-1-11 and 2-6-3 consist of sizeable crystals and contribution from adjacent secondary phases or contamination is less likely.

3.2. Oxygen isotopes

With Δ^{17}O values ranging from -28.4 ± 1.3 to -17.4 ± 0.7‰ (Table 2), the hibonite-rich CAIs are ^{16}O-rich compared to the Earth and show a considerable spread in oxygen isotopes (Fig. 2a). The data scatter around the CCAM line, but many are resolved from and plot to the right of the CCAM line (Fig. 3). The CAIs with the highest Δ^{17}O values plot on the left of the CCAM line (depleted in ^{18}O), but only two of these (2-6-7 and 2-7-5) are resolved from the CCAM line outside of 2σ uncertainty (Fig. 3). While most analyses collected within the same CAI agree within uncertainties, the spot analyses of three CAIs do not agree within uncertainties. As these CAIs could be internally heterogeneous, they are plotted individually in Fig. 2b. No relationship between oxygen isotopic composition and CAI morphology or presence or absence of spinel is apparent in this dataset (Fig. 2c).

3.3. Magnesium isotopes

The majority of hibonite-rich CAIs have δ^{25}Mg values close to 0, but a range of ~7‰ may be present in the dataset (Fig. 4a, Table 3). In the magnesium-three isotope plot, most data are within error of the mass-dependent fractionation line. Therefore, most of the studied CAIs lack excesses in $\delta^{26}Mg^*$ (Table 3) that would attest to a formation in the presence of live ^{26}Al (Fig. 4b). Instead, excursions in $\delta^{26}Mg^*$ are comparable to uncertainties (mostly within ±3‰) for most CAIs. CAIs 2-6-8 and 2-7-4 (red diamonds in Fig. 4a) have the largest $\delta^{26}Mg^*$ values, their model isochrons yield initial ^{26}Al/^{27}Al ratios of $(0.86 \pm 0.33) \times 10^{-5}$ and $(1.54 \pm 0.25) \times 10^{-5}$, respectively. Nearly all studied hibonites have ^{27}Al/^{24}Mg ratios between ~80 and 150; there are only three outliers with higher ratios.

3.4. Calcium and titanium isotopes

The studied hibonite-rich CAIs lack large mass-dependent fractionation effects in calcium and titanium isotopes, but do show a large range of negative and positive anomalies in the neutron(n)-rich isotopes, ^{48}Ca and ^{50}Ti (e.g., approximate range of 240‰ for δ^{50}Ti; Table 4). Most of the studied CAIs fall within a range in δ^{50}Ti (^{46}Ti/^{48}Ti normalization) from approximately −40‰ to +20‰ a cluster of seven CAIs exists at ~+60‰ and two objects have

Table 1
Hibonite mineral chemistry obtained by electron microprobe analysis. In the case of multiple analyses in the same grain, average concentrations are given (in weight percentages, wt%, with uncertainties corresponding to two standard deviations).

Name	N[a]	V[b]	Ions per formula unit						Weight percents					
			Ca^{2+}	Al^{3+}	Mg^{2+}	Ti^{4+}	O^{2-}	Cation Sum	CaO (wt%)	Al_2O_3 (wt%)	MgO (wt%)	TiO_2 (wt%)	FeO (wt%)	Sum (wt%)
		(kV)												
1-1-11	3	15, 20	1.0	11.7	0.1	0.2	19	13.00	8.5 ± 0.2	87.9 ± 1.3	0.8 ± 0.0	1.9 ± 0.7	0.13 ± 0.19	99.3
1-3-2	1	15	1.0	11.2	0.4	0.3	19	13.01	8.4	84.3	2.2	4.1	0.12	99.5
1-4-2	2	15	1.0	11.6	0.2	0.2	19	13.01	8.5 ± 0.2	87.0 ± 0.7	1.0 ± 0.2	2.1 ± 0.6	b.d.	98.6
1-4-3	3	15	1.0	11.7	0.1	0.1	19	13.01	8.6 ± 0.2	88.5 ± 1.6	0.7 ± 0.2	1.4 ± 0.7	b.d.	99.2
1-4-5	4	15	1.0	11.7	0.1	0.1	19	13.00	8.4 ± 0.1	87.6 ± 1.1	0.7 ± 0.1	1.7 ± 0.3	b.d.	98.5
1-5-3	4	15	1.1	11.6	0.1	0.2	19	13.01	8.7 ± 0.4	87.8 ± 1.1	0.9 ± 0.2	2.0 ± 0.8	0.14 ± 0.15	99.6
1-6-1	3	15	1.0	11.7	0.1	0.2	19	13.00	8.5 ± 0.2	88.5 ± 0.9	0.9 ± 0.1	1.9 ± 0.3	b.d.	99.9
1-9-3	1	20	1.0	11.5	0.2	0.2	19	13.00	8.6	87.4	1.2	2.7	b.d.	99.9
1-9-4	2	20	1.0	11.6	0.2	0.2	19	13.00	8.5 ± 0.0	87.8 ± 0.5	1.1 ± 0.0	2.4 ± 0.1	b.d.	99.9
2-2-7	2	20	1.0	11.7	0.1	0.1	19	12.98	8.3 ± 0.1	89.6 ± 1.9	0.6 ± 0.1	1.7 ± 0.0	b.d.	100.3
2-2-9	2	20	1.0	11.7	0.1	0.1	19	13.00	8.5 ± 0.1	89.1 ± 1.4	0.8 ± 0.1	1.7 ± 0.0	b.d.	100.0
2-6-2	2	20	1.0	11.6	0.2	0.2	19	12.99	8.4 ± 0.0	89.1 ± 2.2	1.1 ± 0.2	2.4 ± 0.6	b.d.	101.1
2-6-3	2	20	1.0	11.4	0.3	0.3	19	13.00	8.6 ± 0.1	86.0 ± 1.4	1.6 ± 0.0	3.2 ± 0.2	0.05 ± 0.03	99.5
2-6-5	2	20	1.0	11.6	0.2	0.2	19	13.00	8.6 ± 0.2	88.4 ± 0.1	0.9 ± 0.0	2.2 ± 0.3	b.d.	100.2
2-6-7	2	20	1.0	11.6	0.2	0.2	19	13.00	8.7 ± 0.9	88.7 ± 0.7	1.0 ± 0.1	2.4 ± 0.7	b.d.	100.8
2-6-9	2	20	1.0	11.6	0.2	0.2	19	13.00	8.6 ± 0.0	88.3 ± 1.6	1.0 ± 0.2	2.2 ± 0.7	b.d.	100.1
2-7-1	3	20	1.0	11.7	0.1	0.2	19	12.99	8.5 ± 0.0	89.8 ± 0.6	0.7 ± 0.1	1.9 ± 0.2	b.d.	101.0
2-7-3	3	20	1.0	11.7	0.1	0.2	19	13.00	8.7 ± 0.5	89.3 ± 1.5	0.8 ± 0.6	2.0 ± 0.5	b.d.	100.8
2-7-4	2	20	1.0	11.6	0.2	0.2	19	12.98	8.5 ± 0.1	88.7 ± 0.4	0.9 ± 0.1	2.6 ± 0.1	b.d.	100.7
2-7-5	2	20	1.0	11.7	0.1	0.1	19	13.00	8.5 ± 0.0	90.3 ± 0.5	0.7 ± 0.1	1.4 ± 0.4	b.d.	100.9
2-7-7	2	20	1.0	11.6	0.2	0.2	19	13.00	8.5 ± 0.0	88.9 ± 2.3	0.9 ± 0.3	2.2 ± 0.8	b.d.	100.5
2-8-1	4	15, 20	1.0	11.6	0.2	0.2	19	12.99	8.4 ± 0.2	87.6 ± 0.9	1.0 ± 0.0	2.6 ± 0.2	b.d.	99.7
2-8-2	33	15, 20	1.0	11.6	0.1	0.2	19	12.99	8.5 ± 0.2	88.4 ± 1.0	0.8 ± 0.0	2.1 ± 0.2	b.d.	99.8
2-8-5	2	20	1.0	11.6	0.2	0.2	19	13.00	8.6 ± 0.1	88.6 ± 0.6	1.0 ± 0.2	2.2 ± 0.4	b.d.	100.4
2-9-1	2	20	1.0	11.6	0.2	0.2	19	12.99	8.5 ± 0.0	89.1 ± 1.1	0.9 ± 0.0	2.3 ± 0.1	b.d.	100.8
2-9-2	2	20	1.0	11.6	0.2	0.2	19	12.99	8.5 ± 0.3	88.7 ± 0.2	1.0 ± 0.1	2.4 ± 0.4	b.d.	100.6
2-9-3	2	20	1.0	11.6	0.2	0.2	19	12.98	8.5 ± 0.2	88.0 ± 0.8	1.0 ± 0.1	2.7 ± 0.1	b.d.	100.2
2-9-4	1	20	1.0	11.7	0.2	0.2	19	13.00	8.5	88.8	0.9	2.0	b.d.	100.2
2-9-7	1	20	1.0	11.6	0.2	0.2	19	13.00	8.6	88.5	1.0	2.3	b.d.	100.4

[a] N: Number of analyses.
[b] V: Acceleration voltage.

Table 2
Oxygen isotope measurements for hibonite-rich CAIs. Averages of spot analyses are given for most CAIs, individual analyses are given for three possibly internally heterogeneous grains.

Name	Type[a]	N[b]	$\delta^{18}O$ (‰)	$\delta^{17}O$ (‰)	$\Delta^{17}O$ (‰)
1-1-11	Aggr., sp rim	3	−34.39 ± 2.25	−39.08 ± 0.89	−21.20 ± 0.68
1-3-2	Aggr.	2	−41.42 ± 1.24	−42.73 ± 0.70	−21.19 ± 0.84
1-4-2	Aggr.	2	−42.18 ± 0.85	−46.70 ± 0.92	−24.76 ± 1.13
1-4-3	Stubby	2	−44.98 ± 0.85	−51.82 ± 1.43	−28.43 ± 1.26
1-4-5	Aggr.	2	−45.56 ± 0.85	−48.17 ± 1.15	−24.48 ± 1.13
1-5-3	Aggr.	2	−45.27 ± 1.24	−46.72 ± 1.01	−23.17 ± 0.84
1-6-1	Aggr.	2	−42.55 ± 0.73	−46.32 ± 0.76	−24.20 ± 0.92
1-9-3	Platy w. sp	2	−43.74 ± 0.65	−49.58 ± 0.96	−26.83 ± 0.79
1-9-4	Platy w. sp	2	−43.49 ± 0.50	−46.71 ± 1.24	−24.10 ± 1.09
2-2-7	Unclear	2	−44.17 ± 0.62	−47.95 ± 1.04	−24.98 ± 1.11
2-2-9	Stubby	2	−45.19 ± 0.62	−46.70 ± 1.59	−23.20 ± 1.52
2-6-2	Platy	2	−40.66 ± 0.82	−42.82 ± 0.70	−21.68 ± 0.75
2-6-5	Stubby	2	−35.73 ± 0.64	−40.02 ± 0.96	−21.44 ± 0.84
2-6-7	Stubby	2	−36.01 ± 0.64	−36.15 ± 0.65	−17.42 ± 0.67
2-6-8	Aggr.	3	−42.07 ± 0.57	−44.50 ± 0.56	−22.62 ± 0.57
2-6-9	Aggr.	2	−41.88 ± 0.64	−44.45 ± 0.65	−22.67 ± 0.67
2-7-1	Platy w. sp	2	−40.67 ± 0.72	−46.02 ± 0.59	−24.87 ± 0.63
2-7-3	Platy	3	−39.97 ± 0.86	−43.87 ± 0.73	−23.08 ± 0.51
2-7-4	Platy	2	−32.78 ± 0.72	−40.42 ± 1.79	−23.37 ± 1.85
2-7-5	Unclear	2	−37.74 ± 0.72	−37.16 ± 0.67	−17.54 ± 0.65
2-7-7	Unclear	2	−35.46 ± 0.72	−40.69 ± 0.59	−22.26 ± 0.50
2-8-1	Unclear	2	−37.35 ± 0.50	−38.04 ± 1.24	−18.61 ± 1.09
2-8-2	Platy	2	−34.80 ± 0.65	−39.64 ± 1.48	−21.55 ± 1.18
2-8-5	Stubby	2	−43.08 ± 0.50	−45.93 ± 1.24	−23.53 ± 1.09
2-8-6	Platy	2	−38.10 ± 0.62	−38.80 ± 1.04	−18.99 ± 1.11
2-9-2	Platy	2	−37.76 ± 0.71	−38.99 ± 0.81	−19.36 ± 0.83
2-9-3	Platy	2	−37.61 ± 0.71	−38.89 ± 0.81	−19.34 ± 0.83
2-9-4	Unclear	2	−44.08 ± 0.77	−51.01 ± 0.85	−28.09 ± 0.83
2-9-7	Unclear	2	−35.47 ± 0.72	−41.35 ± 0.59	−22.91 ± 0.50
Possibly internally heterogeneous					
2-9-1	Platy	1	−37.99 ± 0.82	−37.51 ± 1.00	−17.76 ± 1.05
		1	−37.98 ± 0.82	−40.27 ± 1.00	−20.52 ± 1.05
2-9-5	Platy	1	−37.92 ± 0.82	−38.39 ± 1.00	−18.67 ± 1.05
		1	−40.50 ± 0.82	−40.53 ± 1.00	−19.47 ± 1.05
2-6-3	Aggr.	1	−40.60 ± 0.97	−45.40 ± 0.87	−24.28 ± 0.95
		1	−37.54 ± 0.97	−42.71 ± 0.87	−23.19 ± 0.95

[a] Petrologic type, abbreviations: aggr. – aggregate, sp – spinel, w. – with. If unclear: morphology not recognizable.
[b] N is number of individual analyses included in average.

more extreme anomalies (−71 ± 3‰ and 171 ± 4‰, Table 4, Fig. 5). For $\delta^{48}Ca$, most studied hibonite-rich CAIs have values between −30‰ and +30‰ eight CAIs have $\delta^{48}Ca$ values between ~+55‰ and ~+80‰, with six of these defining a cluster at ~+70‰. There are also two grains with more extreme depletions in ^{48}Ca (−43 ± 4‰ and −61 ± 4‰; Table 4).

The choice of the normalization isotope pair for titanium (i.e., $^{46}Ti/^{48}Ti$ vs. $^{49}Ti/^{47}Ti$ normalization) has only a small effect on the calculated $\delta^{50}Ti$ values. Fig. 5a shows that for most studied CAIs, these values agree with each other within uncertainty. However, $^{49}Ti/^{47}Ti$ normalization results in a slight decrease in the magnitude of $\delta^{50}Ti$ for many of the more anomalous CAIs. The lighter calcium and titanium isotopes have δ-values that are mostly within ±5‰ of the terrestrial value (Fig. 6, Table 4), which we consider unresolvable based on comparable scatter in standard analyses (also compare Tables EA.2 and EA.3 in electronic appendix). Thus, in contrast to regular CAIs and bulk meteorites, where there is a well-defined correlation between $\delta^{46}Ti$ and $\delta^{50}Ti$ with a slope of ~0.2 (Trinquier et al., 2009; Zhang et al., 2012), the studied hibonite-rich CAIs do not show this relationship; ^{46}Ti anomalies are minimal—only two exceed 2σ and all are less than 4σ (Table 4, Fig. 6).

4. DISCUSSION

4.1. Classification and comparison with other Murchison hibonites

Similar to PLACs described previously (e.g., Ireland, 1990; Liu et al., 2009, 2012), the CAIs presented here

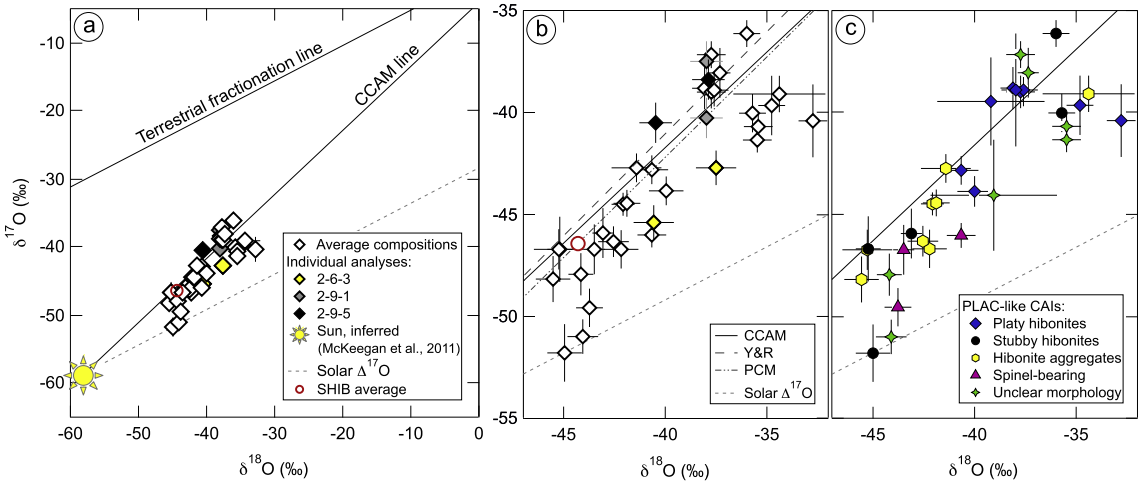

Fig. 2. Oxygen three-isotope diagrams. (a) All studied PLAC-like CAIs are ^{16}O-rich relative to the terrestrial fractionation line, but define a considerable spread in oxygen isotopes. (b) The enlargement of the PLAC-like CAI region from (a) shows that the data scatter around commonly cited lines of slope ~1 (i.e., CCAM; Young & Russell (Y&R), Young and Russell, 1998; and primitive chondrule mixing (PCM), Ushikubo et al., 2012). For comparison, the average composition of 36 SHIBs analyzed in the same session is plotted as well. (c) The color-coding shows that there is no obvious relationship between morphology and oxygen isotopes for the studied CAIs. Plots (a) and (b) show the average oxygen isotopic compositions from multiple analyses in the same PLAC-like CAIs, except for grains 2-6-3, 2-9-1 and 2-9-5, for which individual analyses are plotted as they may be heterogeneous in oxygen isotopes. In (c), average compositions are plotted for all PLAC-like CAIs. (For interpretation of the references to color in this figure legend, the reader is referred to the web version of this article.)

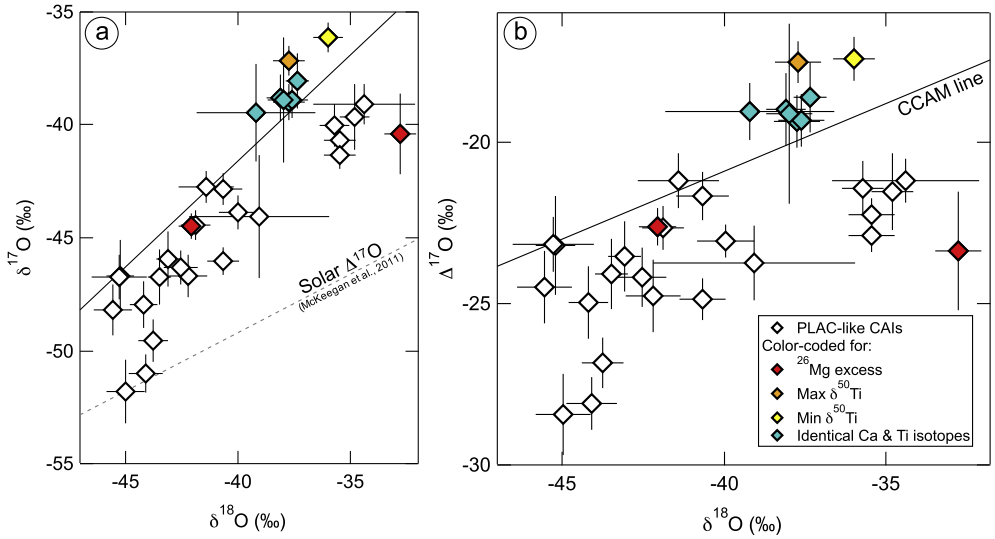

Fig. 3. Oxygen isotopes in PLAC-like CAIs. (a) Same as Fig. 2c, but with color-coding indicating other isotopic properties (i.e., red corresponds to PLAC-like CAIs with the highest $\delta^{26}Mg^*$ values, orange and yellow to the largest positive and negative anomalies in ^{50}Ti, respectively, blue to six grains with indistinguishable calcium and titanium isotopic compositions). The same color-coding is used in subsequent figures. (b) This $\Delta^{17}O$ versus $\delta^{18}O$ plot shows the data as well as the CCAM line. If the precursors (e.g., solids or gases) of these CAIs were initially on the CCAM line, subsequent processing resulted in isotopically light characters only for CAIs with enhanced $\Delta^{17}O$ values (yellow and orange diamonds, possibly also blue diamonds), while processing imprinted isotopically heavy signatures on many CAIs with low $\Delta^{17}O$. (For interpretation of the references to color in this figure legend, the reader is referred to the web version of this article.)

consist predominantly of hibonite, show a large range of δ^{50}Ti and δ^{48}Ca values, lack large radiogenic excesses in ^{26}Mg and show limited variation in magnesium contents (i.e., ^{27}Al/^{24}Mg ratios were typically 80–180; Fig. 4b). These characteristics were found in hibonite-rich CAIs with a variety of morphologies (Fig. 2c, Tables 2–4), i.e., single hibonite crystals ranging from platy to equant, hibonite aggregates, and objects in which hibonite is associated with spinel (usually margins or rims of spinel). Petrologically similar inclusions have been classified as PLACs by other authors (Ireland, 1988, 1990; Liu et al., 2009, 2012). But since two-thirds of the CAIs studied here do not exhibit platy morphologies, we classify these CAIs collectively as *PLAC-like CAIs*. The observation that most PLAC-like

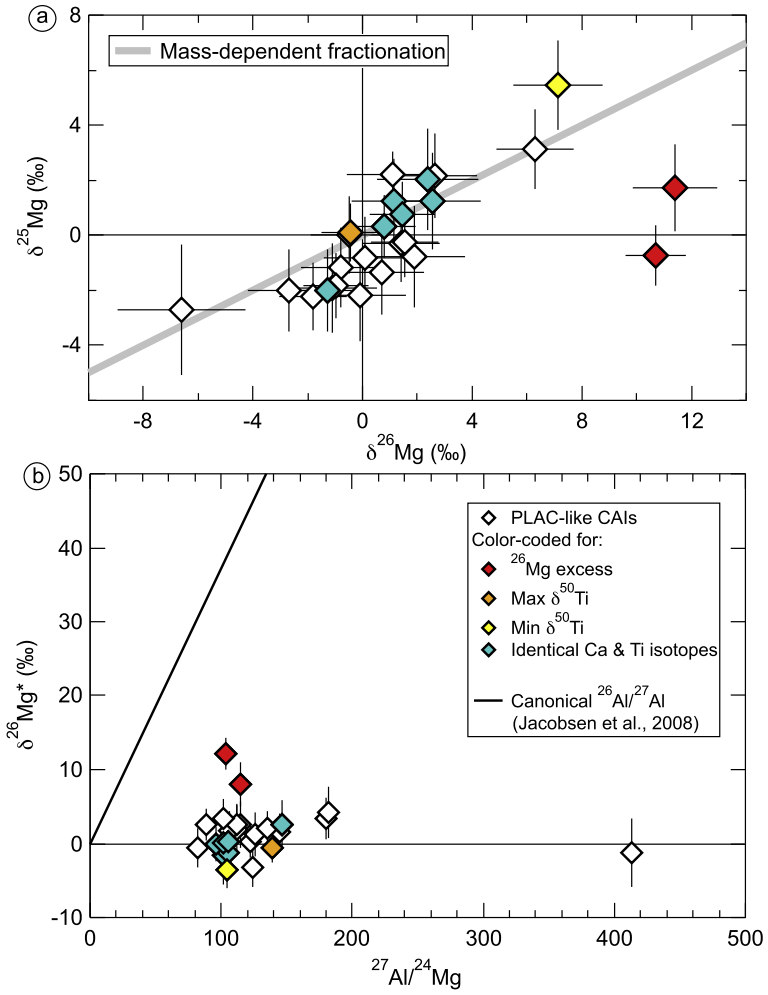

Fig. 4. (a) Magnesium three-isotope diagram. Most PLAC-like CAIs show only small degrees of variation in ^{25}Mg and ^{26}Mg and plot within uncertainty of the line defined by mass-dependent fractionation processes. Only two PLAC-like CAIs (red) show clear enrichments in ^{26}Mg relative to the array, possibly due to radioactive decay of ^{26}Al. (b) All spot analyses of PLAC-like CAIs fall below the isochron defined by CAIs with a canonical abundance of ^{26}Al (MacPherson et al., 2012). Most PLAC-like CAIs have $\delta^{26}Mg^*$ values within uncertainty of 0‰, a few have values that are marginally resolved from 0‰, consistent with formation in a ^{26}Al-free or -poor environment. Only two CAIs (red diamonds) have larger positive $\delta^{26}Mg^*$ values, which could be a result of incorporation of ^{26}Al or nucleosynthetic magnesium anomalies. (For interpretation of the references to color in this figure legend, the reader is referred to the web version of this article.)

CAIs are not platy is consistent with the common description of PLACs as crystal fragments, which implies they have broken off larger crystals or aggregates. Six PLAC-like CAIs studied here have identical isotopic compositions in all four elements (within 2σ uncertainty; blue diamonds in Figs. 2d, 4, 6 and 7), which also supports the idea that many single crystals may have been liberated from larger objects by fragmentation, alteration on the parent body and/or sample preparation processes like disaggregation and in some cases acid treatment.

The four hibonite-rich CAIs that are associated with spinel were classified as PLAC-like CAIs instead of SHIBs because their isotopic properties closely resemble those of PLAC-like CAIs (Figs. 2c and 5). Hibonite grains in these CAIs also have uniformly low magnesium contents, similar to hibonite grains in spinel-free PLAC-like CAIs and different from SHIB hibonites (locally, magnesium contents in some SHIB hibonite grains may be similarly low, but such grains are usually strongly zoned; Fig. A.2). A clear difference between PLAC-like CAIs and SHIBs that were studied in the same sessions is that PLAC-like CAIs show a larger range and clear offsets from the CCAM line, while all SHIBs cluster near the CCAM line at a $\Delta^{17}O$ of ~−23‰ (e.g., Kööp et al., 2016).

4.2. Mass-dependent fractionation and nucleosynthetic effects in PLAC-like CAIs

4.2.1. Oxygen isotopes

This study confirms the spread in $\Delta^{17}O$ found in the most recent study of PLACs or PLAC-like CAIs (Liu et al., 2009). The observed range (−28‰ to −17‰) is more restricted and on average more ^{16}O-rich than $\Delta^{17}O$ values of ^{26}Al-poor FUN and F CAIs, which extend to ~0‰ (e.g., Krot et al., 2008, 2010, 2014, 2015).

Table 3
Al–Mg isotope analyses, including $^{26}Al/^{27}Al$ ratios inferred from model isochrons. An anorthite standard was used for normalization.

Name	Type[a]	Phase[b]	Session[c]	Cycles[d]	$\delta^{25}Mg$ (‰)	$\delta^{26}Mg$ (‰)	$^{27}Al/^{24}Mg$ (‰)	$\delta^{26}Mg^*$ (‰)	$^{26}Al/^{27}Al$ (10^{-5})
1-1-11	Aggr., sp rim	Hib	July 14	20	2.2 ± 0.8	1.1 ± 1.7	123.9 ± 2.4	−3.3 ± 2.6	−0.4 ± 0.3
1-4-2	Aggr.	Hib	July 14	20	−0.3 ± 1.4	1.4 ± 1.4	111.5 ± 1.7	2.0 ± 3.4	0.2 ± 0.4
1-4-3	Stubby	Hib	Feb 14	39	−0.8 ± 1.8	1.9 ± 1.8	180.2 ± 2.7	3.4 ± 2.8	0.3 ± 0.2
1-4-5	Aggr.	Hib	July 14	20	−1.2 ± 1.5	−0.8 ± 1.5	144.5 ± 2.1	1.5 ± 2.5	0.1 ± 0.2
1-5-3	Aggr.	Hib	July 14	20	−0.8 ± 1.5	0.1 ± 1.5	106.1 ± 2.2	1.7 ± 2.6	0.2 ± 0.3
1-6-1	Aggr.	Hib	July 14	20	−1.8 ± 1.2	−1.0 ± 1.2	111.5 ± 2.3	2.6 ± 2.6	0.3 ± 0.3
1-9-3	Platy w. sp	Hib	Feb 14	37	−1.4 ± 1.5	0.7 ± 1.5	101.4 ± 2.9	3.3 ± 2.6	0.5 ± 0.4
2-2-7	Unclear	Hib	July 14	20	−2.2 ± 1.7	−0.1 ± 1.7	181.6 ± 2.5	4.2 ± 3.4	0.3 ± 0.3
2-2-9	Stubby	Hib	July 14	20	−2.0 ± 1.5	−2.7 ± 1.5	125.9 ± 1.8	1.2 ± 3.0	0.1 ± 0.3
2-6-2	Platy	Hib	July 14	20	0.0 ± 1.4	−0.5 ± 1.4	81.8 ± 1.6	−0.5 ± 2.7	−0.1 ± 0.5
2-6-5	Stubby	Hib	July 14	20	2.2 ± 1.5	2.6 ± 1.5	102.2 ± 2.0	−1.6 ± 2.5	−0.2 ± 0.3
2-6-7	Stubby	Hib	Feb 14	39	5.4 ± 1.6	7.1 ± 1.6	104.0 ± 1.8	−3.5 ± 2.5	−0.5 ± 0.3
2-6-8	Aggr.	Hib	July 14	20	1.7 ± 1.6	11.4 ± 1.6	114.6 ± 1.8	8.1 ± 3.1	1.0 ± 0.4
2-7-1	Platy w. sp	Hib	July 14	20	−0.3 ± 1.3	1.6 ± 1.3	135.1 ± 2.3	2.0 ± 2.3	0.2 ± 0.2
2-7-3	Platy	Hib	July 14	20	−2.7 ± 2.4	−6.6 ± 2.4	413.0 ± 5.3	−1.3 ± 4.6	0.0 ± 0.2
2-7-4	Platy	Hib	July 14	39	−0.7 ± 1.1	10.7 ± 1.1	103.3 ± 1.4	12.1 ± 2.2	1.6 ± 0.3
2-7-5	Unclear	Hib	July 14	39	0.1 ± 1.1	−0.4 ± 1.1	139.2 ± 1.4	−0.7 ± 2.1	−0.1 ± 0.2
2-8-1	Unclear	Hib	Feb 14	39	1.2 ± 1.8	2.5 ± 1.8	101.6 ± 1.4	0.2 ± 2.6	0.0 ± 0.4
2-8-2	Platy	Hib	July 14	20	3.1 ± 1.4	6.3 ± 1.4	122.1 ± 1.8	0.2 ± 2.2	0.0 ± 0.3
2-8-5	Stubby	Hib	July 14	20	−1.9 ± 1.6	−1.1 ± 1.6	114.3 ± 1.7	2.6 ± 3.1	0.3 ± 0.4
2-8-6	Platy	Hib	July 14	20	2.0 ± 1.8	2.4 ± 1.8	101.8 ± 1.2	−1.6 ± 3.9	−0.2 ± 0.5
2-9-1	Platy	Hib	July 14	39	0.3 ± 1.1	0.8 ± 1.1	105.2 ± 1.6	0.2 ± 2.1	0.0 ± 0.3
2-9-2	Platy	Hib	July 14	20	1.2 ± 1.5	1.2 ± 1.5	105.3 ± 2.1	−1.3 ± 2.8	−0.2 ± 0.4
2-9-3	Platy	Hib	July 14	39	0.8 ± 1.2	1.4 ± 1.2	96.5 ± 1.4	−0.1 ± 2.3	0.0 ± 0.3
2-9-4	Unclear	Hib	July 14	39	−2.2 ± 1.2	-1.8 ± 1.2	88.9 ± 1.4	2.5 ± 2.2	0.4 ± 0.3
2-9-5	Platy	Hib	July 14	20	−2.0 ± 1.5	−1.3 ± 1.5	146.5 ± 1.8	2.6 ± 3.3	0.3 ± 0.3

[a] Petrologic type with abbreviations as in Table 1.
[b] Phase analyzed.
[c] SIMS analysis session.
[d] Number of cycles.

The resolved $\Delta^{17}O$ variations among PLAC-like CAIs are in clear contrast to regular CAIs as defined in Section 1. The trend of the PLAC-like CAI data is along the CCAM line and therefore resembles trends described by some CAIs and Wark-Lovering (WL) rims from the altered CV3.6 chondrite Allende (e.g., Clayton et al., 1977; Simon et al., 2011; Park et al., 2012). However, recent studies focused on CAIs and WL rims from the least metamorphosed chondrites commonly have found more uniform compositions close to the common $\Delta^{17}O$ values of −23‰; this indicates that most of the variations found in Allende CAIs may have resulted from mineral-dependent exchange with or remelting in a ^{16}O-poor reservoir (Krot et al., 2009; Bodénan et al., 2014). Similarly, our high spatial resolution analyses of a large number of SHIBs revealed that their $\Delta^{17}O$ range is more restricted (−24.5 ± 1.0 to −22.0 ± 0.8‰; Kööp et al., 2016) than previously thought (−27‰ to −16‰; Liu et al., 2009). Yet, PLAC-like CAIs we analyzed and prepared under identical conditions as SHIBs show a $\Delta^{17}O$ range of ~11‰ and thus substantiate the inferences that: (1) PLAC-like CAIs are distinct from regular CAIs and SHIBs in oxygen isotopes; and (2) while the oxygen isotopic composition may have been uniform during formation of regular CAIs, considerable variations existed during formation of PLAC-like CAIs.

The distribution of PLAC-like CAIs (Liu et al., 2009; this study) is largely consistent with a line of slope ~1 in the oxygen-three isotope diagram (e.g., CCAM, PCM (Ushikubo et al., 2012), and Young & Russell (Young and Russell, 1998) lines), similar to more evolved (i.e., more homogeneous) chondritic components like Allende CAIs and chondrules. However, we also find resolved deviations to both sides of the CCAM line in some PLAC-like CAIs (Figs. 2 and 3). Most of these are displaced towards heavier compositions relative to the CCAM line (right side), but at least two grains are isotopically light (Figs. 2 and 3). Six hibonite grains (blue diamonds in Fig. 3) also plot to the left but overlap with the CCAM line within 2σ uncertainty. These six grains may have been liberated from the same CAI (see Section 4.1) and their clustering to the left of the CCAM line could indicate that they are isotopically light. These excursions from a single mixing line are unlikely to be due to instrumental or secondary effects (for a thorough discussion, see Appendix A.2). Instead, the deviations could reflect mass-dependent fractionation processes associated with their formation, i.e., condensation and melt evaporation (Richter et al., 2002). However, it is unclear why PLAC-like CAIs would show a relationship between $\Delta^{17}O$ and mass-fractionation effects. Furthermore, there is no correlation between the magnitude of oxygen isotopic deviation from the CCAM line and $\delta^{25}Mg$ (Tables 2 and 3), which might be expected for condensation or evaporation. Alternatively, deviations from a single mixing

Table 4
Calcium and titanium isotope data, the latter is given in two commonly used normalizations ($^{46}Ti/^{48}Ti$ and $^{49}Ti/^{47}Ti$) to facilitate comparisons with other studies and materials. The data listed here is corrected by sample-standard bracketing and a Rayleigh law. Internally corrected data using the exponential law can be found in Electronic Appendix Table EA.2.

Name	C[a]	$\delta^{47}Ti$ (‰)	$\delta^{49}Ti$ (‰)	$\delta^{50}Ti$ (‰)	F_{Ti}[b] (‰/amu)	$\delta^{46}Ti$ (‰)	$\delta^{48}Ti$ (‰)	$\delta^{50}Ti$ (‰)	F_{Ti} (‰/amu)	$\delta^{42}Ca$ (‰)	$\delta^{43}Ca$ (‰)	$\delta^{48}Ca$ (‰)	F_{Ca} (‰/amu)
		$^{46}Ti/^{48}Ti$ normalization[c]				$^{49}Ti/^{47}Ti$ normalization				$^{40}Ca/^{44}Ca$ normalization			
1-1-11	Cleavage	0.7 ± 5.2	2.1 ± 3.9	9.7 ± 6.8	−1.2 ± 3.3	0.4 ± 4.3	−1.7 ± 4.7	6.3 ± 9.1	−0.2 ± 2.6	−0.1 ± 3.0	0.4 ± 2.2	19.8 ± 6.8	−0.1 ± 0.4
1-4-2	Pv, cleavage	−0.5 ± 5.2	−2.1 ± 3.9	5.4 ± 6.9	0.8 ± 3.3	−0.3 ± 4.2	1.4 ± 4.8	8.9 ± 9.3	−0.1 ± 2.6	v2.8 ± 3.0	−0.5 ± 1.9	−3.6 ± 6.5	0.2 ± 0.4
1-4-3		0.0 ± 5.3	−2.9 ± 4.1	4.5 ± 6.9	0.1 ± 3.3	−0.8 ± 4.4	1.4 ± 4.9	8.9 ± 9.5	−1.3 ± 2.7	−3.6 ± 3.0	−0.4 ± 2.2	−8.7 ± 6.5	−0.3 ± 0.4
1-4-5	Pv, cleavage	−1.3 ± 5.1	−2.3 ± 3.9	3.2 ± 6.8	0.8 ± 3.3	0.6 ± 4.2	1.8 ± 4.8	6.1 ± 9.2	0.3 ± 2.6	−3.3 ± 2.9	−1.4 ± 2.0	−4.7 ± 6.6	−0.3 ± 0.4
1-5-3	Boundary	−2.9 ± 2.7	−3.8 ± 2.8	−39.9 ± 3.0	2.5 ± 1.2	2.2 ± 2.9	3.4 ± 2.8	−35.3 ± 4.3	2.0 ± 1.2	−3.1 ± 2.7	−4.5 ± 3.2	−43.4 ± 4.1	0.2 ± 1.0
1-6-1		−0.1 ± 2.1	−1.3 ± 2.3	4.5 ± 3.1	2.3 ± 1.2	−0.5 ± 2.9	0.7 ± 2.0	6.4 ± 3.9	1.6 ± 1.2	−0.5 ± 2.4	−0.6 ± 3.3	−0.1 ± 3.3	0.4 ± 0.5
2-2-7	Crack	−0.7 ± 5.1	−1.5 ± 4.0	0.4 ± 7.0	−0.5 ± 3.3	0.2 ± 4.4	1.3 ± 4.8	2.5 ± 9.3	−1.1 ± 2.6	−1.5 ± 2.9	0.6 ± 2.1	−5.5 ± 6.6	0.6 ± 0.4
2-2-9		−2.8 ± 5.1	−2.1 ± 3.9	−7.2 ± 6.7	1.1 ± 3.3	3.3 ± 4.3	2.4 ± 4.8	−5.3 ± 9.1	1.5 ± 2.6	−3.6 ± 3.0	−2.8 ± 2.2	−17.4 ± 6.5	−0.6 ± 0.4
2-6-2	Crack	−0.9 ± 2.0	2.4 ± 2.4	18.8 ± 3.4	1.2 ± 1.0	2.5 ± 2.6	−0.6 ± 2.3	14.9 ± 4.6	2.8 ± 1.2	−1.2 ± 4.7	0.3 ± 2.7	15.0 ± 4.4	0.7 ± 1.0
2-6-5	Pv	−0.7 ± 2.2	4.3 ± 2.4	9.5 ± 2.9	−0.7 ± 1.2	3.3 ± 3.0	−1.8 ± 2.2	2.6 ± 4.2	1.8 ± 1.3	1.8 ± 2.4	0.9 ± 3.5	27.1 ± 3.7	−0.2 ± 0.5
2-6-7	Pv	−2.1 ± 2.0	−1.5 ± 2.2	−71.3 ± 3.0	−1.4 ± 1.0	2.3 ± 2.3	2.0 ± 2.3	−70.1 ± 4.2	−1.1 ± 1.2	0.9 ± 4.9	1.6 ± 2.9	−61.2 ± 3.9	−0.6 ± 1.0
2-6-8	Pv	2.6 ± 2.0	0.9 ± 2.3	−18.1 ± 3.3	−1.8 ± 1.0	−3.5 ± 2.2	−1.6 ± 2.2	−18.1 ± 4.3	−2.7 ± 1.2	−1.0 ± 4.9	0.2 ± 2.7	−20.4 ± 4.2	1.0 ± 1.0
2-7-3	Pv	3.2 ± 2.7	−1.7 ± 3.0	−26.8 ± 3.8	−1.8 ± 1.2	−5.8 ± 3.2	−0.7 ± 2.8	−22.8 ± 5.8	−4.2 ± 1.5	−0.8 ± 3.1	0.3 ± 2.9	−23.9 ± 5.1	2.1 ± 0.7
2-7-4		1.0 ± 1.6	4.9 ± 1.8	58.5 ± 2.8	−0.2 ± 0.7	1.0 ± 2.2	−2.9 ± 1.9	51.3 ± 4.7	1.8 ± 1.2	0.5 ± 3.2	1.5 ± 2.8	81.2 ± 5.7	−0.3 ± 0.6
2-7-5	SIMS pit	0.3 ± 2.1	6.2 ± 2.5	171.0 ± 4.0	−0.2 ± 0.9	2.8 ± 2.6	−3.2 ± 2.3	160.4 ± 6.0	2.7 ± 1.3	−3.0 ± 3.1	0.4 ± 3.1	56.5 ± 5.7	−0.3 ± 0.7
2-8-1		0.3 ± 2.0	5.5 ± 2.1	62.2 ± 3.0	0.2 ± 0.9	2.4 ± 2.2	−2.9 ± 2.1	53.6 ± 4.3	2.8 ± 1.0	−1.1 ± 2.3	0.0 ± 3.6	71.1 ± 5.5	−0.6 ± 0.5
2-8-2		0.2 ± 2.1	4.0 ± 2.1	14.3 ± 2.9	−2.1 ± 1.0	2.0 ± 2.4	−2.1 ± 2.2	8.4 ± 4.3	−0.1 ± 1.1	3.2 ± 2.4	2.3 ± 3.6	31.5 ± 5.1	−0.2 ± 0.5
2-8-5		−0.7 ± 1.9	−3.8 ± 2.1	−8.6 ± 3.3	2.5 ± 1.0	−1.1 ± 2.2	2.7 ± 2.1	−2.6 ± 4.3	0.6 ± 1.1	−2.7 ± 4.8	−0.7 ± 2.5	−18.0 ± 4.0	1.3 ± 1.0
2-8-6		−0.4 ± 2.1	2.4 ± 2.6	60.4 ± 2.8	1.1 ± 0.8	2.1 ± 2.4	−1.0 ± 2.3	56.3 ± 4.2	2.6 ± 1.1	0.1 ± 2.4	−0.1 ± 3.0	70.0 ± 4.5	−0.7 ± 0.9
2-9-1	Crack	0.7 ± 2.2	3.4 ± 2.4	64.6 ± 3.3	1.9 ± 1.3	0.6 ± 2.9	−2.0 ± 2.1	59.3 ± 4.1	3.2 ± 1.2	−1.6 ± 2.6	0.3 ± 3.4	70.7 ± 3.8	−0.2 ± 0.5
2-9-2	Crack	−0.1 ± 2.0	5.4 ± 2.3	64.2 ± 3.2	1.4 ± 1.2	2.6 ± 2.8	−2.6 ± 1.9	55.7 ± 4.2	4.1 ± 1.2	0.8 ± 2.5	1.8 ± 3.3	72.6 ± 3.5	−0.3 ± 0.5
2-9-3	Cleavage	1.1 ± 2.0	2.0 ± 2.1	61.2 ± 3.2	3.4 ± 1.2	−0.6 ± 2.8	−1.6 ± 1.9	58.5 ± 3.8	3.9 ± 1.1	−0.9 ± 2.5	−0.9 ± 3.4	69.7 ± 3.5	0.2 ± 0.5
2-9-4	Pv	0.5 ± 2.1	−0.8 ± 2.6	−2.0 ± 3.2	2.1 ± 1.3	−1.1 ± 2.9	0.1 ± 2.1	−0.6 ± 4.3	1.5 ± 1.3	−1.0 ± 2.7	−1.0 ± 3.7	−0.3 ± 3.5	0.6 ± 0.5
2-9-5	Epoxy	0.0 ± 2.0	3.4 ± 2.3	60.5 ± 3.1	2.2 ± 1.2	1.8 ± 2.9	−1.7 ± 2.0	55.1 ± 4.1	3.9 ± 1.2	−0.4 ± 2.5	−0.9 ± 3.4	71.9 ± 3.6	−0.2 ± 0.5
1-9-3	Pv	1.3 ± 1.8	−0.1 ± 2.1	−4.5 ± 2.7	1.7 ± 0.7	−1.9 ± 2.2	−0.8 ± 2.0	−3.9 ± 4.3	1.1 ± 1.1	−1.5 ± 3.1	−0.3 ± 3.2	−4.0 ± 5.4	0.8 ± 0.7
2-7-1		1.0 ± 2.0	−0.9 ± 2.0	−0.6 ± 2.9	2.4 ± 0.7	−1.9 ± 2.3	0.0 ± 2.2	1.2 ± 4.6	1.4 ± 1.2	−0.8 ± 3.1	0.6 ± 3.1	5.6 ± 5.3	0.7 ± 0.7

[a] Description of imperfections found in analysis pit post SIMS. Abbreviations: Pv – perovskite, RMN – refractory metal nugget.
[b] Intrinsic fractionation in Ti.
[c] Favored normalization for Ti isotopes.

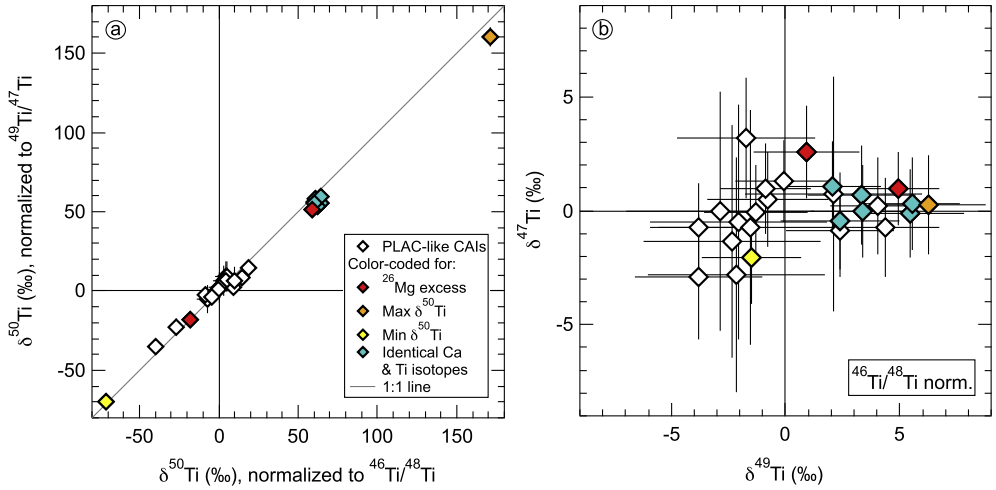

Fig. 5. (a) This figure illustrates the effects of choosing different normalization pairs on δ^{50}Ti values. While most PLAC-like CAIs plot on or within uncertainty of the 1:1 line (i.e., the magnitude of δ^{50}Ti values is not significantly affected by choosing ^{46}Ti/^{48}Ti or ^{49}Ti/^{47}Ti normalization), the magnitudes are typically slightly smaller in ^{49}Ti/^{47}Ti normalization, particularly for grains with larger anomalies. (b) The δ^{47}Ti versus δ^{49}Ti plot shows that the spread in δ^{47}Ti appears to be smaller than in δ^{49}Ti.

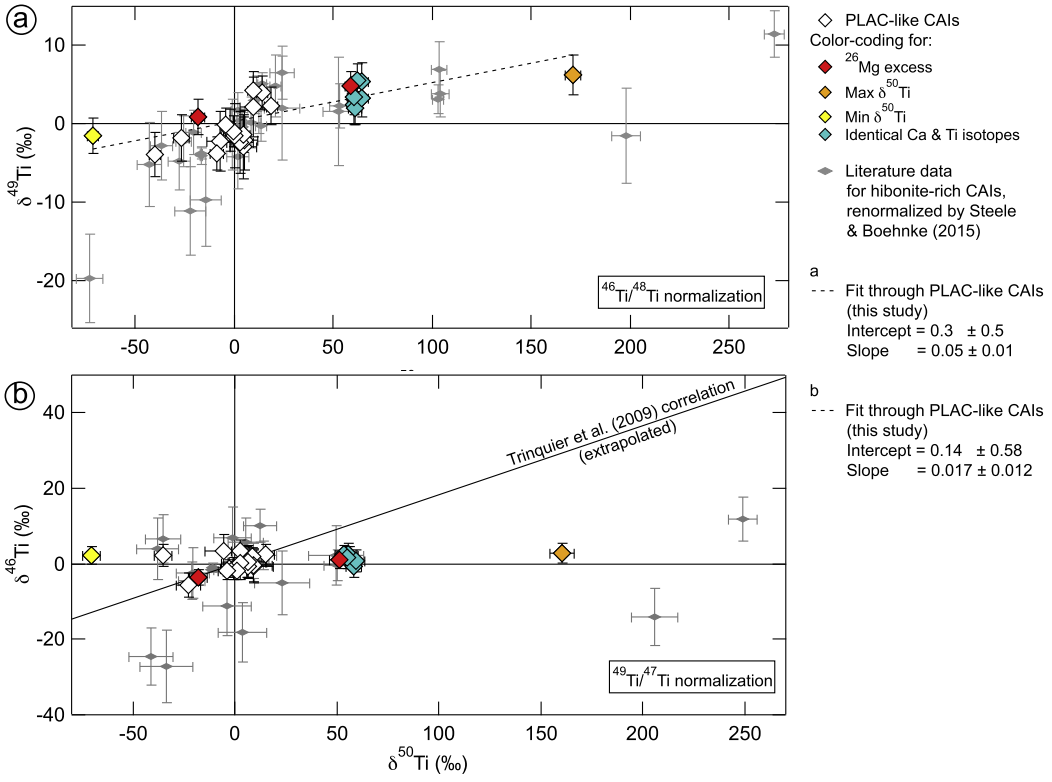

Fig. 6. Comparison of ^{50}Ti anomalies with effects in ^{49}Ti (a) and ^{46}Ti (b). (a) δ^{49}Ti and δ^{50}Ti correlate in sign (^{46}Ti/^{48}Ti normalization). (b) In ^{49}Ti/^{47}Ti normalization, δ^{46}Ti and δ^{50}Ti values do not correlate for most PLAC-like CAIs. Both the CAIs studied here as well as literature data for PLACs deviate from the extrapolated correlation line defined by more homogeneous solar system materials (Trinquier et al., 2009). However, some of the data with smaller anomalies in ^{50}Ti ($|\delta^{50}\text{Ti}| \leqslant \sim 25‰$) appears to plot on the correlation line. Literature data is from Steele and Boehnke (2015) and references therein and limited to grains labeled 'PLACs'.

line could represent mixing between distinct anomalous nucleosynthetic oxygen components. The origin of these oxygen isotopic variations is discussed in more detail in Section 4.3.

4.2.2. Magnesium isotopes

With an average inferred ^{26}Al/^{27}Al ratio of $(1.7 \pm 1.6) \times 10^{-6}$, PLAC-like CAIs are not only ^{26}Al-poor relative to many regular CAIs, but also appear to have formed

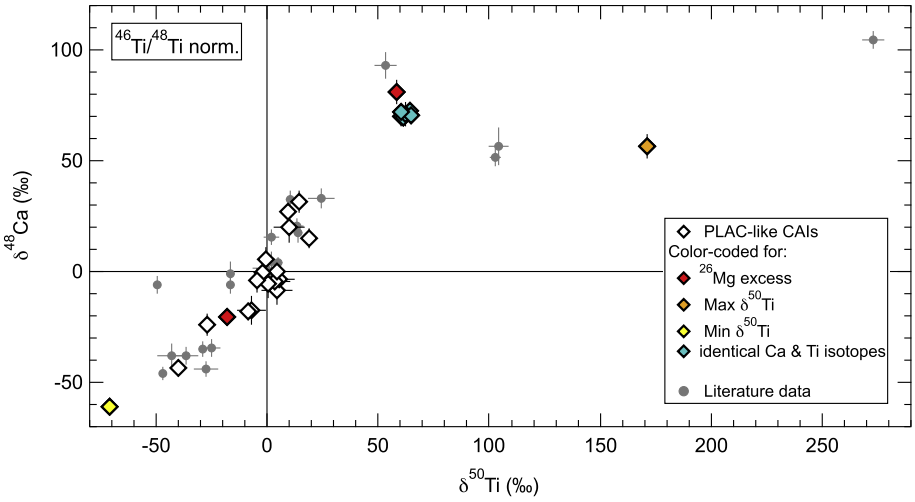

Fig. 7. The graph shows the large enrichments and depletions in ^{48}Ca and ^{50}Ti in PLAC-like CAIs. The titanium data are normalized to ^{46}Ti/^{48}Ti, the calcium data to ^{40}Ca/^{44}Ca. The range and distribution of the dataset is similar to previous studies. Literature data for PLACs are compiled from Zinner et al. (1986, 1987), Fahey et al. (1987a,b), Ireland (1990), Sahijpal et al. (2000) and Liu et al. (2009).

from material with a ^{26}Al/^{27}Al ratio below the Galactic background level of $\sim 8 \times 10^{-6}$ (Diehl et al., 2006). Only two CAIs have enhanced $\delta^{26}Mg^*$ values (2-6-8 and 2-7-4, with 8.0 ± 6.0‰ and 12.1 ± 2.2‰, respectively) that could be consistent with ^{26}Al incorporation close to the Galactic background level (model ^{26}Al/^{27}Al ratios of $\sim(10–15) \times 10^{-6}$). While the PLAC-like CAIs investigated show excursions to positive $\delta^{26}Mg^*$ values, negative $\delta^{26}Mg^*$ values are only marginally resolved (the lowest value is -3.5 ± 2.5‰, 2σ). This is in contrast to previous studies, which found resolved negative $\delta^{26}Mg^*$ values (down to -6 ± 2‰; Liu et al., 2012). When combined with the data from Liu et al. (2012), PLAC-like CAIs may indicate magnesium isotopic variability on the order of 15–20‰ in the early solar system, assuming that the positive $\delta^{26}Mg^*$ values reflect magnesium isotopic variability, not ^{26}Al decay. Whether this assumption is realistic is evaluated in Section 4.4.

Most PLAC-like CAIs cluster around a δ^{25}Mg of 0 (Fig. 4a). However, the data were normalized to an anorthite glass standard as the only available hibonite standard has significantly higher magnesium contents than the PLAC hibonites. Since the matrix effect could have introduced a small, consistent bias in δ^{25}Mg and δ^{26}Mg, no significance can be placed on the absolute values. However, the spread within the dataset is likely real (Fig. 4a). All PLAC-like CAIs except CAIs 2-6-8 and 2-7-4 plot within 2σ uncertainty of the mass-fractionation line (Fig. 4a). Therefore, we refrain from assigning significance to poorly defined trends the dataset, but encourage reinvestigation of the magnesium isotopic systematics in PLAC-like CAIs with a new, possibly synthetic standard that is a better match to the chemistry of PLAC hibonite.

4.2.3. Calcium and titanium isotopes

The 2σ uncertainties listed in Table 4 for calcium and titanium isotope measurements obtained with the CAMECA IMS-1280 (3–7‰ for both δ^{50}Ti and δ^{48}Ca) are comparable to previous studies of similar CAIs using other instruments (CAMECA IMS-3f: ~1–6‰ for δ^{50}Ti, ~3–6‰ for δ^{48}Ca, Ireland, 1990; 3–5‰ for δ^{50}Ti, Fahey et al., 1987a; CAMECA IMS-1270: ~7–9‰ for δ^{50}Ti, Liu et al., 2009). But while previous studies applied the exponential law to correct for instrumental and intrinsic fractionation simultaneously (internal correction), our data was corrected for instrumental fractionation using sample-standard bracketing and for intrinsic fractionation by applying a Rayleigh law (Zhang et al., 2014). As uncertainties of bracketing standard measurements were propagated, the resulting uncertainties are larger than for internally corrected data. As outlined in the Appendix A.3, the new approach is preferable because (1) it is doubtful that both instrumental and intrinsic fractionation follow the exponential law (Park et al., 2014; Zhang et al., 2014); and (2) the larger resulting uncertainties likely reflect the true uncertainty of our measurements more accurately. However, Appendix A.3 demonstrates that the two approaches yield indistinguishable δ-values within 2σ uncertainties and that direct comparison with internally corrected literature data is therefore possible. For reference, Electronic Appendix Table EA.2 shows our data internally corrected with the exponential law.

Similar to previous studies, the ranges in δ^{50}Ti and δ^{48}Ca values are large and the anomalies tend to agree in sign (Fig. 7), consistent with a common nucleosynthetic origin of these nuclides. The data show clear deviations from a two-component mixing line, which is consistent with previous studies of similar types of CAIs (Zinner et al., 1986, 1987; Fahey et al., 1987a,b; Ireland, 1990; Sahijpal et al., 2000; Liu et al., 2009). Such a distribution could be a result of mixing a distinct isotopically anomalous carrier phase (fixed Ca/Ti ratio, e.g., perovskite as suggested by Dauphas et al., 2014) into a chemically heterogeneous nebula reservoir, or by mixing multiple carrier phases (variable Ca/Ti ratios) into a chemically homogeneous or heterogeneous nebula. Since both the range and the distribution resemble previous studies, we conclude, like previous

authors, that the dataset is consistent with a heterogeneous distribution of neutron-rich material, probably originating from a Type Ia supernova, in a reservoir depleted in this component compared to solar (e.g., Hinton et al., 1987).

Anomalies in the lighter isotopes of calcium and titanium are either small or unresolved in the studied PLAC-like CAIs (Fig. 6, Table 4). Some PLAC-like CAIs have anomalies in ^{49}Ti or ^{46}Ti when normalized to ^{46}Ti/^{48}Ti or ^{49}Ti/^{47}Ti, respectively. Previous studies concluded that the anomaly was in ^{49}Ti and thus normalized to ^{46}Ti/^{48}Ti (e.g., Fahey et al., 1985; Ireland, 1988, 1990; Liu et al., 2009). But recent evidence for correlated anomalies in ^{46}Ti and ^{50}Ti (^{49}Ti/^{47}Ti normalization) in CV CAIs, bulk chondrites and achondrites (Trinquier et al., 2009) suggests that an anomalous ^{46}Ti component existed in the early solar system and could also be present in PLAC-like CAIs. However, many PLAC-like CAIs deviate from the extrapolated correlation line (Fig. 6b) and the degree of variability in δ^{46}Ti (~10‰) is smaller than expected (~40‰) based on the Trinquier et al. correlation and the magnitude of effects in δ^{50}Ti. These results could suggest that the anomalous ^{46}Ti component was not present in the PLAC formation reservoir or that homogenization affected the anomalous carriers of ^{50}Ti and ^{46}Ti differently between formation of PLAC-like and CV CAIs. However, literature data renormalized by Steele and Boehnke (2015) reveals a δ^{46}Ti range of approximately 40‰ in PLAC-like CAIs, which is comparable to the predicted range for these CAIs (~60‰, given the larger range of δ^{50}Ti effects in literature data). These results suggest that the ^{46}Ti component may have been present in the formation reservoir of PLACs, but was initially decoupled from the ^{50}Ti component. PLAC-like CAIs with small anomalies ($|\delta^{50}\text{Ti}| \leqslant 25$‰) studied here fall on the Trinquier et al. correlation line (Fig. 6b), which could indicate that PLAC-like CAIs with smaller anomalies formed after onset of the process responsible for the coupling of ^{50}Ti and ^{46}Ti in the early solar system. However, this coupling is not observed for PLACs with similar anomalies in the renormalized literature data (Steele and Boehnke, 2015; Fig. 6b). For additional discussion regarding the choice of normalization isotopes for PLAC-like CAIs, see Appendix A.4.

Finally, we note that similar to previous studies (e.g., Ireland, 1990), the PLAC-like CAIs show no significant intrinsic fractionation in calcium and titanium isotopes, precluding that these highly refractory materials formed by extensive melt evaporation of primitive precursors.

4.3. A link between oxygen isotopes and large-scale nucleosynthetic anomalies and its implications

The studied PLAC-like CAIs show a link between oxygen isotopes and the magnitude of nucleosynthetic anomalies (Fig. 8). Large positive and negative anomalies in ^{50}Ti and ^{48}Ca only occur in CAIs with ^{16}O-poor compositions relative to the Sun, and the ranges in δ^{50}Ti and δ^{48}Ca values decrease as the CAIs become ^{16}O-enriched, resulting in a triangular distribution in Fig. 8. Some of the data are clustered; the cluster at a Δ^{17}O of ~−19‰ in Fig. 8 may be the result of sampling multiple fragments of a larger CAI that

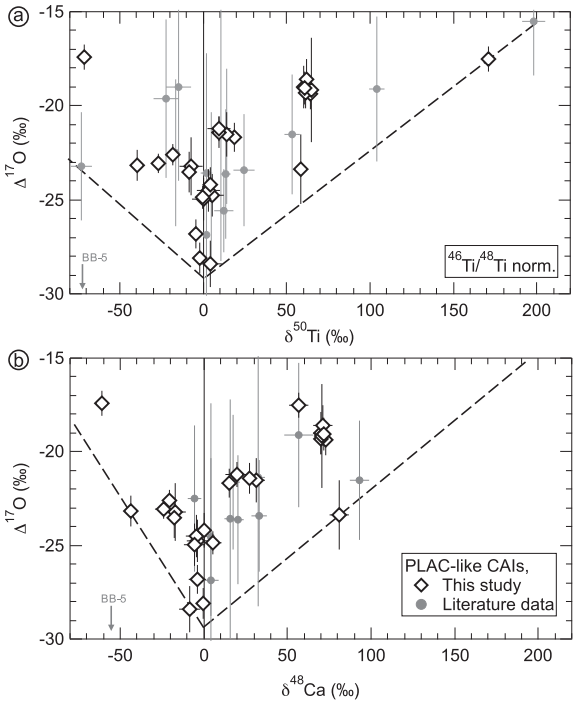

Fig. 8. The PLAC-like CAIs show a relationship between the magnitude of nucleosynthetic anomalies in (a) ^{50}Ti and (b) ^{48}Ca and the enrichment in ^{16}O. ^{16}O-rich CAIs lack sizeable anomalies and the range of anomalies increases with increasing Δ^{17}O values. The dashed lines indicate the lower bound of the distribution of PLAC-like CAIs. Arrows point to the composition of hibonite-corundum spherule BB-5. Literature data for PLACs and BB-5 were compiled from Fahey et al. (1987a) and references therein, Ireland (1990), Ireland et al. (1992), Sahijpal et al. (2000), and Liu et al. (2009).

broke apart (see Section 4.1). In contrast, another possible cluster exists at Δ^{17}O ~−22‰, but δ^{48}Ca values show a considerable spread (~+15‰ to +40‰; Fig. 8b), suggesting these grains could have sampled nebula material with similar oxygen but variable calcium isotopic characteristics. Both the ^{16}O-rich, isotopically normal and most of the ^{16}O-poor, isotopically anomalous PLAC-like CAIs appear to have avoided incorporation of significant levels of ^{26}Al (compare Figs. 4 and 8).

Literature data for PLAC-like CAIs are generally consistent with a triangular distribution (Fig. 8; data compiled from Fahey et al. (1987a,b, and references therein), Ireland (1990), Ireland et al. (1992), Sahijpal et al. (2000) and Liu et al. (2009)). Combined, these data fan out approximately symmetrically to negative and positive δ^{50}Ti and δ^{48}Ca values with increasing Δ^{17}O (indicated by dashed lines in Fig. 8). The hibonite-corundum CAI BB-5 plots outside of the triangular distribution defined by PLAC-like CAIs (i.e., $\Delta^{17}\text{O} = -32 \pm 4$‰, $\delta^{48}\text{Ca} = -56 \pm 4$‰, $\delta^{50}\text{Ti} = -72 \pm 2$‰; Fahey et al., 1987a), potentially challenging its significance. However, the mineralogy of BB-5 is distinct from PLAC-like CAIs, suggesting that it formed under different conditions (and different location or time) and could have sampled a different isotopic reservoir than PLAC-like CAIs. Given that the triangular distribution is

defined by a large number of PLAC-like CAIs (literature data and this study), it seems unlikely that it is coincidental.

Below, we explore a number of scenarios that could explain the link between nucleosynthetic anomalies and oxygen isotopes in PLAC-like CAIs. This interpretation is challenging as oxygen isotopic compositions of gases and solids in the early solar system are unknown and models make conflicting assumptions and predictions. For example, nebular self-shielding models typically assume that at time zero, CO, H_2O and dust had uniform compositions (i.e., solar $\Delta^{17}O$; Clayton, 2002; Lyons and Young, 2005), while Krot et al. (2010) suggest that the solar nebula gas (i.e., $CO + H_2O$) was enriched in ^{16}O and primitive dust was ^{16}O-poor relative to the Sun. Furthermore, isotopic self-shielding may have occurred in the parent molecular cloud, and models predict that the isotopic composition of material falling onto the forming protoplanetary disk was likely variable in time (Lee et al., 2008; Yang et al., 2011). Unless otherwise stated, we assume that the inferred $\Delta^{17}O$ value for the Sun (~−28‰; McKeegan et al., 2011) represents the average composition of the solar nebula. From this perspective, the most ^{16}O-rich PLAC-like CAIs, which lack anomalies in calcium and titanium isotopes, can be viewed as isotopically normal in oxygen and refractory elements, while the ^{16}O-poor ones are viewed as isotopically anomalous in oxygen. In addition, we assume that PLAC-like CAIs formed prior to regular CAIs, based on considerations described in Section 1.

4.3.1. A nucleosynthetic link between anomalies in oxygen, calcium and titanium

The link between oxygen isotopes and anomalies in ^{48}Ca and ^{50}Ti in PLAC-like CAIs could be a result of mixing between a solar component ($\Delta^{17}O$ of ~−28‰, $\delta^{50}Ti$ and $\delta^{48}Ca$ of ~0‰) and distinct presolar carrier phases with isotope anomalies in all three elements. Such a mixing model requires at least two distinct ^{16}O-poor components (one enriched, the other depleted in both ^{50}Ti and ^{48}Ca). We consider this scenario unlikely for two reasons. First, the symmetry of the distribution calls for two complementary components, which seems coincidental given that other titanium, calcium or magnesium isotopes do not show comparable effects (Figs. 4 and 6). Second, it is difficult to identify suitable sources for the two components. For example, type Ia supernovae (SN) are not expected to produce ^{50}Ti- and ^{48}Ca-rich oxide grains (see Dauphas et al., 2010) and while Type II SN may produce ^{16}O-poor material with depletions and enrichments in ^{50}Ti, such material should have enrichments in ^{46}Ti. In addition, ^{48}Ca is not produced in these SN (Rauscher et al., 2002).

4.3.2. Symmetry-dependent fractionation of oxygen isotopes

Since it is unlikely that the variations in oxygen, calcium, and titanium isotopes were introduced by the presolar components with anomalies in all three elements, we now consider separate origins for the variations in $\Delta^{17}O$ and refractory elements. For oxygen, chemical reactions can introduce symmetry-dependent fractionation (e.g., Thiemens, 2006). Such reactions could have taken place in the solar nebula and would have resulted in both sub- and supersolar $\Delta^{17}O$ values in oxygen-bearing species. Any aberration from the solar value would then indicate that the material experienced processing. As we expect that unprocessed material is more likely to retain nucleosynthetic anomalies than processed materials, it is unclear why large anomalies would be associated with nonsolar (i.e., processed) oxygen isotopic compositions in PLAC-like CAIs. While symmetry-dependent fractionation of oxygen isotopes cannot be excluded, we see no direct support for this scenario in the dataset.

4.3.3. Isotopic self-shielding

Isotopic self-shielding is another process often considered to explain the $\Delta^{17}O$ variations of solar system materials (e.g., Clayton, 2002; Yurimoto and Kuramoto, 2004; Lyons and Young, 2005). Nebular self-shielding models assume that prior to its initiation, dust and gas had solar $\Delta^{17}O$ values. Upon onset of self-shielding, ^{16}O-rich CO and ^{16}O-poor H_2O reservoirs are hypothesized to have formed, resulting in an isotopic zonation of nebular H_2O and CO that likely varied in time (Clayton, 2002; Lyons and Young, 2005). To account for the link between $\Delta^{17}O$ and anomalies in ^{50}Ti and ^{48}Ca, isotopically anomalous precursors could have equilibrated with ^{16}O-poor H_2O, while isotopically uniform precursors either avoided equilibration, or fully equilibrated with both ^{16}O-rich CO and ^{16}O-poor H_2O. Based on these considerations, three scenarios can be explored to explain the isotopic characteristics of PLAC-like CAIs.

(1) Thermal processing: ^{16}O-rich PLAC-like CAIs may have experienced high degrees of thermal processing resulting in a solar $\Delta^{17}O$ due to full equilibration with both ^{16}O-rich CO and ^{16}O-poor H_2O and efficient dilution of isotopic anomalies in refractory elements (e.g., during full volatilization and recondensation of dust). In contrast, ^{16}O-poor, isotopically anomalous PLAC-like CAIs could have experienced lower degrees of processing that did not result in efficient dilution of anomalies and only allowed for oxygen isotopic exchange with ^{16}O-poor H_2O, but not ^{16}O-rich CO.

(2) Temporal $\Delta^{17}O$ variations: Nebular regions may have experienced a rise and fall in the $\Delta^{17}O$ of H_2O (Lyons and Young, 2005). If PLAC-like CAIs formed over an extended period of time, they may have tracked the initial evolution of H_2O from solar to ^{16}O-poor compositions. However, the link between $\Delta^{17}O$ values and the degree of heterogeneity in ^{50}Ti and ^{48}Ca would then suggest that their formation region evolved from an isotopically homogenized to a highly heterogeneous state (indicated by dashed arrows in Fig. 9a). Alternatively, if PLAC-like CAIs tracked the fall of $\Delta^{17}O$, the relationship in Fig. 8 would be consistent with PLAC-like CAIs having formed in a nebula that experienced continuous homogenization of nucleosynthetic anomalies (i.e., highly anomalous ^{16}O-poor PLAC-like CAIs formed prior to ^{16}O-rich, homogeneous PLAC-like CAIs; solid arrows in Fig. 9). However, this scenario

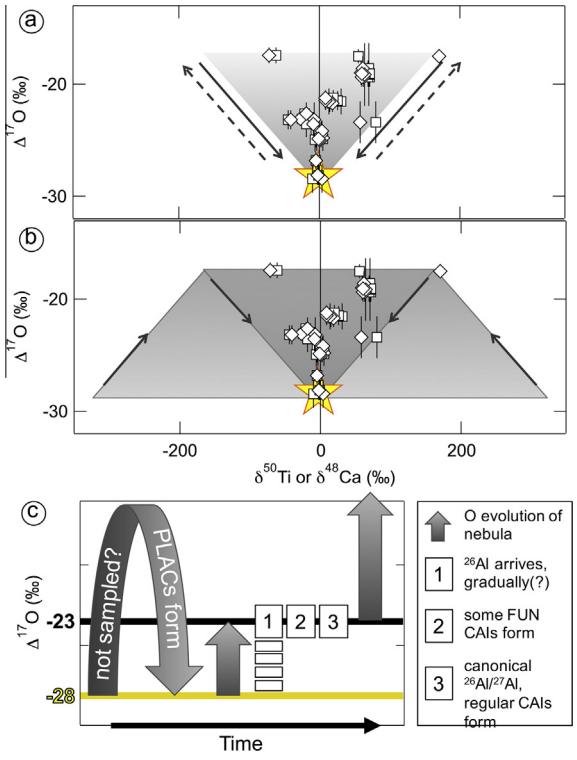

Fig. 9. Illustration of the chronological explanations for the link between oxygen isotopes and anomalies in ^{48}Ca (squares) and ^{50}Ti (diamonds). (a) Arrows indicate how the degree of isotopic heterogeneity in the CAI formation would have changed if PLAC-like CAIs formed either while Δ^{17}O values were increasing (dashed arrows, e.g., due to self-shielding) or decreasing (solid arrows). (b) Illustration of the nonuniform oxygen isotopic evolution of the nebula inferred if a chronology is assigned based on the degree of isotopic heterogeneity in refractory elements. Assuming that the nebula started with a solar oxygen isotopic composition and that mixing processes continuously homogenized nucleosynthetic anomalies, the data would suggest that the CAI formation region evolved from a solar oxygen isotopic composition to a Δ^{17}O of −17‰ or higher (this phase was not sampled by PLAC-like CAIs). Then, the first PLAC-like CAIs formed, recording elevated Δ^{17}O values and large anomalies in ^{48}Ca and ^{50}Ti. The dataset then indicates that while the CAI formation was becoming increasingly homogenized in refractory elements, it also became continuously enriched in ^{16}O, returning to a solar Δ^{17}O. (c) The nonuniform oxygen isotopic evolution of the CAI formation region inferred from PLAC-like, regular and FUN CAIs. After the initial reversal and evolution of the CAI formation region to a Δ^{17}O of ~−28‰ as inferred in (b), a second reversal may have resulted in an evolution to a Δ^{17}O of ~−23‰ before a canonical distribution of ^{26}Al was achieved, as indicated by FUN and other fractionated CAIs with low ^{26}Al/^{27}Al ratios and small or unresolved nucleosynthetic anomalies (Park et al., 2013, 2014; Kööp et al., 2015). The CAI formation region may have remained or fluctuated around a Δ^{17}O of ~−23‰ until a canonical abundance had been achieved and regular CAIs formed.

would likely require a subsequent reversal and evolution to a Δ^{17}O value of ~−23‰ to account for the compositions of regular CAIs if they formed after PLAC-like CAIs in the same region (Fig. 9c).

(3) Radial Δ^{17}O variations: The predicted radial zonation in the Δ^{17}O of nebular H_2O (Clayton, 2002; Lyons and Young, 2005) may have allowed PLAC-like CAIs to inherit different Δ^{17}O values if they or their precursors formed at different distances from the Sun. For example, at larger distances, precursors of ^{16}O-poor, anomalous CAIs may have formed as aggregates of ^{16}O-poor H_2O ice and unprocessed, isotopically anomalous dust. In contrast, the more isotopically uniform, ^{16}O-rich PLAC-like CAIs may have formed closer to the Sun in a region that was not affected by self-shielding. Higher ambient temperatures near the Sun and mixing during a possibly longer transit through the disk could account for the isotopically uniform compositions of these CAIs. However, this model would require that PLAC-like CAIs with indistinguishable chemical and morphological characteristics could form at both small and large distances from the Sun (e.g., shock waves) or that the ^{16}O-poor, icy anomalous precursors migrated inward and were transformed into CAIs in the hot regions close to the Sun while preserving the isotopic properties of both ice and dust. The latter scenario might be complicated by the different condensation temperatures of ice and dust (silicate and oxide). As ice is expected to evaporate during transit before reaching the CAI formation region, the volatilized H_2O could have fractionated from the dust phase, mixed with more ^{16}O-rich CO and H_2O in the inner solar system, leaving behind ^{16}O-rich, anomalous dust.

In summary, if isotopic self-shielding was responsible for the oxygen isotopic variations in PLAC-like CAIs, a number of scenarios could be invoked that may explain the link between oxygen isotopes and the degree of isotopic heterogeneity in refractory elements. The newly established systematics should be taken as additional constraints for the early isotopic evolution of the solar nebula.

4.3.4. Presolar reservoirs model

As an alternative to self-shielding, the relationship between oxygen isotopes and ^{48}Ca and ^{50}Ti anomalies could be the result of a physical link between anomalous presolar phases and a ^{16}O-poor reservoir. As both calcium and titanium are refractory elements (Grossman, 1972; Lodders, 2003) and are thus present in solids over a large range of nebula temperatures, this ^{16}O-poor reservoir may have been the primordial solar nebular dust. In this model, large anomalies in ^{48}Ca and ^{50}Ti would have been caused by a heterogeneous distribution of anomalous isotopic carriers in the unprocessed dust reservoir. If unprocessed nebular dust was ^{16}O-poor compared to the Sun, the nebular gas (likely $CO + H_2O$) must have been relatively enriched in ^{16}O (Fig. 10a). These considerations are similar to a model proposed by Krot et al. (2010) that explains the difference in Δ^{17}O between the Sun and terrestrial planets and asteroids as a result of isotopically distinct presolar dust and gas reservoirs. The model suggests that variations in Δ^{17}O result from exchange between the dust and gas reservoirs

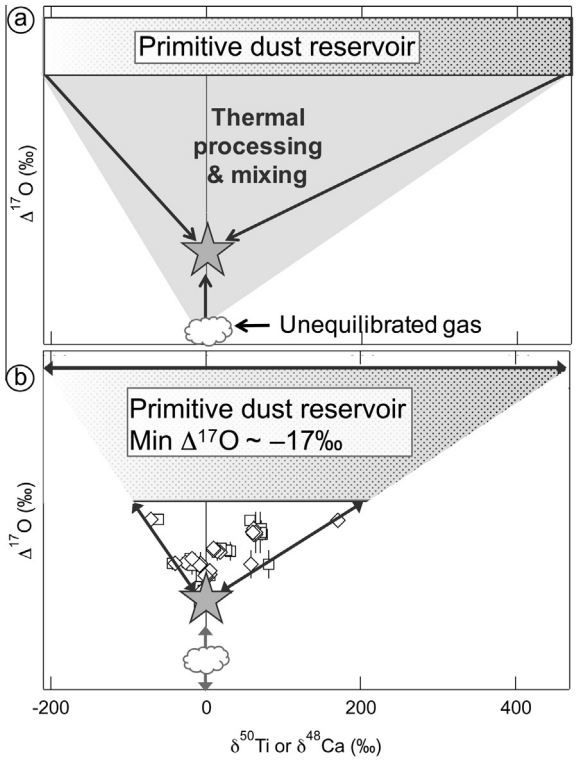

Fig. 10. Illustration of the presolar reservoirs model based on Krot et al. (2010), but extended to explain the compositions of PLAC-like CAIs. Initially, the solar system's oxygen is present in two distinct reservoirs, i.e., ^{16}O-rich gas (cloud symbol) and ^{16}O-poor primordial dust (gray band, e.g., at $\Delta^{17}O = 0‰$). The dust spans a range of anomalies in ^{48}Ca and ^{50}Ti because of heterogeneous distribution of neutron-rich carrier phase(s) in the dust reservoir (indicated by pattern in primitive dust band). (a) Complete equilibration between dust and gas leads to a solar $\Delta^{17}O$ and homogenization of nucleosynthetic anomalies (star symbol). (b) The compositions of the PLAC-like CAIs (diamonds for ^{50}Ti, squares for ^{48}Ca) can be explained by mixing between equilibrated and primitive dust. The data constrains a lower limit for the $\Delta^{17}O$ value of the primitive dust (−17‰).

during thermal processing (Fig. 10a). Assuming that anomalies in ^{50}Ti and ^{48}Ca are efficiently diluted by such thermal processing, the triangular distribution (Fig. 8) found in PLAC-like CAIs could be explained if they formed as mixtures between highly processed and unprocessed dust. Unprocessed dust would be ^{16}O-poor with large variations in ^{50}Ti and ^{48}Ca (Fig. 10b), while highly processed dust had no or minimal anomalies in refractory elements and a solar $\Delta^{17}O$ if it equilibrated with the gas reservoir at a solar dust-to-gas ratio.

The assumption that thermal processing results in efficient dilution of nucleosynthetic anomalies in calcium and titanium isotopes is in contrast to a model proposed by Trinquier et al. (2009). Specifically, Trinquier et al. (2009) propose that preferential volatilization of less-stable anomalous carriers and subsequent fractionation of gas from remaining dust could have created isotopically anomalous reservoirs. However, the refractory nature of calcium and titanium suggests that they would be among the last elements to evaporate and among the first elements to recondense, which may limit the efficiency of thermal processing as a mechanism for creating isotopic anomalies in these elements. Instead, we expect that thermal processing (e.g., complete volatilization and recondensation) was efficient in homogenizing isotopic anomalies in a poorly mixed reservoir. For PLAC-like CAIs, the anomalies are likely a result of heterogeneous distribution of ^{50}Ti and ^{48}Ca enriched carriers from a Type Ia SN in a reservoir that was depleted in these isotopes (Hinton et al., 1987; Section 4.2.3). Type Ia SN ejecta are likely among the most fragile presolar components (coatings on preexisting ISM grains (Nozawa et al., 2011) or small, reactive metal grains), and were likely susceptible to being destroyed and diluted by the thermal processes that lead to oxygen isotope exchange between gas and dust (see Huss et al., 2003, for a discussion on mineralogy-dependent loss of presolar carriers due to nebular thermal processing). This may also be the reason why this presolar component has yet to be isolated and identified in a meteorite.

If distinct presolar oxygen isotopic components were present and heterogeneously distributed in the primordial dust reservoir, the presolar reservoirs model can also account for the observed deviations from a single mixing line in oxygen isotopes (Fig. 3a). This interpretation is supported by studies of presolar oxide and silicate grains, which are on average ^{16}O-poor and show additional variation in ^{17}O and ^{18}O (e.g., Nittler et al., 2008). In the absence of mass-dependent fractionation, the dataset would be expected to fan out symmetrically to both sides of a mixing line defined by the average compositions of the primordial gas and dust reservoirs. This is not observed in the PLAC-like CAIs (Fig. 2b), possibly because of contributions from mass-dependent isotope fractionation (e.g., due to melt evaporation). This could also be the reason why PLAC-like CAIs with solar $\Delta^{17}O$ are displaced from the CCAM line. However, it is not known whether the composition of the Sun, and therefore the composition of completely equilibrated dust, is on or displaced from the CCAM line (McKeegan et al., 2011). The possibility of nucleosynthetic oxygen isotope anomalies complicates the interpretation of calculated $\Delta^{17}O$-values. In $\Delta^{17}O$ notation, deviations of nucleosynthetic origin to the left (^{18}O-poor or ^{17}O-rich) or right (^{18}O-rich or ^{17}O-poor) of a slope-one line would be interpreted as lower or higher enrichment in ^{16}O, respectively, while the anomalies are actually in ^{18}O or ^{17}O. However, the fluctuations around a slope-one line are too small to affect the triangular distribution in Fig. 8 significantly.

Finally, we note that the isotopic composition of BB-5 (Fahey et al., 1987a; Fig. 8) is not directly consistent with the model as this inclusion is ^{16}O-rich in spite of being highly depleted in ^{48}Ca and ^{50}Ti. This may require additional processing (e.g., the CAI might have equilibrated with the ^{16}O-rich gas reservoir after formation at high temperatures) or could be an indicator against the presolar reservoirs model. Reanalysis of BB-5 with modern instrumentation is desirable.

4.4. The degree of isotopic heterogeneity at the time of introduction of ^{26}Al

Most PLAC-like CAIs show a mutual exclusivity relationship between potential radiogenic ^{26}Mg excesses and anomalies in ^{50}Ti and ^{48}Ca (e.g., Clayton et al., 1988; Ireland, 1988; Liu et al., 2009; this work), suggesting that the concentration of ^{26}Al was low in their formation region. PLAC-like CAIs 2-6-8 and 2-7-4 have considerable anomalies, but also enhanced $\delta^{26}Mg^*$ values (~10‰; red diamonds in Figs. 4–7), possibly indicative of ^{26}Al incorporation at a level of $(1–1.5) \times 10^{-5}$. However, positive $\delta^{26}Mg^*$ values can also result from magnesium isotopic heterogeneity (excesses in ^{26}Mg and ^{24}Mg, or depletions in ^{25}Mg). Based on their position relative to other PLAC-like CAIs in Fig. 4a, excesses in ^{26}Mg are more likely than in ^{24}Mg, which allows for both radiogenic and nucleosynthetic origins. If the excesses are radiogenic, they could be (1) due to admixture of fresh ^{26}Al that eventually resulted in a canonical $^{26}Al/^{27}Al$ ratio of $\sim 5 \times 10^{-5}$ in regular CAIs or (2) small heterogeneities in the background level of ^{26}Al. If fresh ^{26}Al was admixed into the CAI formation region while PLAC-like CAIs formed (1), more of these CAIs should show positive $\delta^{26}Mg^*$ values and $\delta^{26}Mg^*$ variations should be larger. This is contrary to observations. Instead, small fluctuations in the distribution of the ^{26}Al background may be possible, as the model $^{26}Al/^{27}Al$ for 2-6-8 and 2-7-4 are only slightly larger than the Galactic background level (Diehl et al., 2006).

5. CONCLUSIONS

(1) Our study confirms the ^{26}Al-poor character of PLAC-like CAIs, the large range of anomalies in ^{50}Ti and ^{48}Ca (>100‰) as well as the range in Δ^{17}O from solar (~−28‰) to ~−17‰. However, the higher precision achieved in this study reveals deviations from the CCAM line, mostly to the right, but in at least two cases also to the left of the line. We primarily ascribe these deviations from a two-component mixing line to nucleosynthetic effects in oxygen isotopes rather than solely to signatures of condensation and evaporation.

(2) Our study reveals a new, systematic relationship between the Δ^{17}O value and the magnitude of ^{50}Ti and ^{48}Ca anomalies in these ^{26}Al-poor CAIs, which could suggest a physical link between anomalous ^{48}Ca and ^{50}Ti carriers and a ^{16}O-poor reservoir. The distribution could be a result of varying degrees of equilibration between isotopically distinct inherited presolar dust and gas reservoirs, similar to a model proposed by Krot et al. (2010). However, the data can also be explained in the context of isotopic self-shielding, but seems to require additional conditions to be met (e.g., prolonged formation of these objects, reversals in the oxygen isotopic evolution of the CAI formation region, transient heating events in colder nebula regions, or different degrees of thermal processing).

(3) The 26 PLAC-like CAIs studied for titanium isotopes lack the large variations in ^{46}Ti that would be expected by extrapolation from the variation in solar system materials that formed after arrival of ^{26}Al (Trinquier et al., 2009). This may suggest that the anomalous ^{46}Ti and ^{50}Ti components were initially decoupled.

(4) Small fluctuations in $\delta^{26}Mg^*$ exist in PLAC-like CAIs and may be the result of magnesium isotopic heterogeneity or ^{26}Al decay. While we conclude that PLAC-like CAIs formed prior to arrival of fresh ^{26}Al that led to a canonical abundance in regular CAIs, small $\delta^{26}Mg^*$ variations could be due to variations in the ^{26}Al background level.

(5) PLAC-like CAIs appear to record an era of solar nebular history prior to isotopic homogenization and introduction of ^{26}Al and may be the oldest object to have formed in the solar system.

ACKNOWLEDGEMENTS

We thank Christine Floss, Ming-Chang Liu, and two anonymous reviewers for their insightful comments that greatly improved the paper. Editorial handling by Munir Humayun was greatly appreciated. We also thank Ian Steele for assistance with electron microprobe analyses and Nicolas Dauphas and Michael Foote for helpful discussions. L. Kööp and A.M. Davis were funded by the NASA Cosmochemistry Program (grant NNX09AG39G, to A.M. Davis) and NASA Laboratory Analysis of Returned Samples Program (grant NNX15AF78G, to A.M. Davis). L. Kööp was also supported through a NASA Earth and Space Science Fellowship. N.T. Kita acknowledges funding from the NASA Cosmochemistry Program (grants NNX11AG62G, NNX14AG29G). A.N. Krot acknowledges funding from the NASA Cosmochemistry and Emerging Worlds Programs (grants NNX10AH76G and NNX15AH38G). WiscSIMS is partly supported by NSF (EAR03-19230, EAR10-53466, EAR13-55590). P.R. Heck acknowledges funding from the Tawani Foundation.

APPENDIX A

A.1. Preparing flat epoxy grain mounts for small samples

Most SIMS applications require preparation of samples that have a minimal profile over a large surface area (<10 μm variation in the inner 7 mm of a polished mount; Kita et al., 2009). This is necessary as changes in the relative elevation of analysis areas result in distortions of the electric field lines that lead to additional instrumental mass-fractionation, which cannot be corrected for using standards. To avoid these effects, grains or rock fragments can be cast in the center of one-inch epoxy rounds, which are then polished flat and coated with a conductive material (e.g., gold or carbon). For small samples (<~30 μm), it is difficult to mount multiple grains in a single mount because they need to be placed at the same level, otherwise polishing leads to loss of samples and/or exposure of only part of the mounted samples. If samples are precious, a common approach is thus mounting and polishing small grains individually or depositing them on or pressing them into metal

mounts. Preparing samples in individual mounts is inconvenient for SIMS analyses as it requires frequent sample changes, and preparation in metal mounts can be highly labor intensive because grains need to be polished individually prior to pressing them into the metal if flat surfaces are required.

Therefore, we have developed a new technique that allows mounting of multiple small or thin samples in the same mount. The approach presented here has worked very well for preparing the thin, platy hibonite crystals for analysis, but it was also used to mount larger samples (>1 mm).

For this technique which is illustrated in Fig. A1, a cleaned, thick (>1 mm) microscope slide is attached to a steady surface (e.g., an aluminum block works well). Using a cleaned razor blade, a piece of thin one-sided tape is smoothly attached to the slide and the aluminum block (commercially available, clear acetate packaging tape was found to work well), with the sticky side facing down. No air bubbles should be trapped between the glass and the tape. The tape surface is then cleaned and dried. Using a clean hair, a thin line of epoxy is applied to the center of the slide covered with tape. The samples (cleaned and dried) are then placed on the epoxy lines. If grains are very small (<5 μm), it was found to be good practice to first place the grain on the line, but then push the grains off the line so they were only attached to the tape by the minimal amount of epoxy adhering to the grain. After attaching all grains to the tape surface, commercially available one-inch ring molds were added (and fixed to the tape using a layer of clay on the outside), the assemblage was covered with a clean beaker and the epoxy was left to cure for 3–4 h at room temperature (this was a fraction of the required curing time of ~24 h). We then filled the molds with freshly prepared epoxy. After curing, the mount can be easily removed from the tape. Grains are usually already partially exposed, only a small amount of polishing is necessary to fully expose small grains. We therefore polished the mounts by hand, often using a combination of lapping film and polishing pads, starting at a 6 or 9 μm grid, but the grid size needs to be adjusted based on the size of the samples mounted. Frequent checks of the polishing progress under a petrographic microscope are required.

The main advantages of the described technique are (1) easy removal of the cured epoxy round from the tape, (2) extremely flat surface of the epoxy round even prior to polishing, (3) only minimal amounts of the epoxy need to be removed to fully expose small grains, (4) the tape is flat enough that multiple small samples can be mounted on the same level and evenly exposed during polishing. We have tested this for samples that are as thin as ~5 μm. More tests are necessary to determine the minimum grain size this approach can be used for.

A.2. Evaluation of possible instrumental and secondary effects on oxygen and magnesium isotopes

The PLAC-like CAIs show deviations from the CCAM line to both lighter and heavier compositions and a small, yet resolvable spread in magnesium isotopes (~7‰ amu^{-1}). These variations could be indicative of the formation processes of PLAC-like CAIs or of oxygen and magnesium isotopic heterogeneity in the early solar system (see Sections 4.2.1 and 4.2.2), but could also be a result of improper correction of measured isotope ratios by SIMS.

Due to mass-dependent fractionation processes inside the mass spectrometer, measured isotope ratios typically deviate from true ratios. For the oxygen and magnesium isotopes in Figs. 2 and 4, these deviations would result in

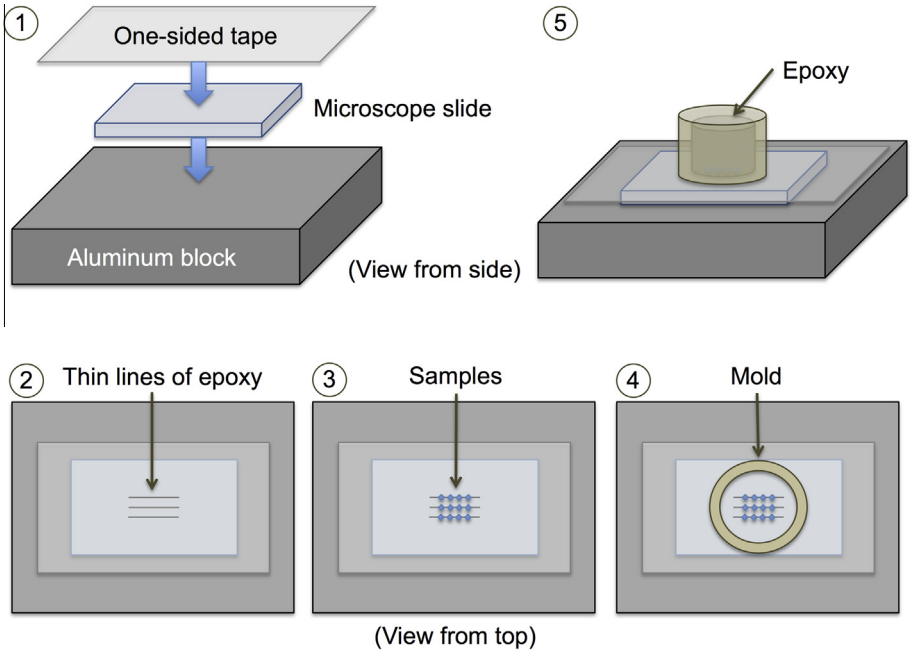

Fig. A1. Illustration of major steps required for the preparation of flat grain mounts of micron-sized samples (described in text).

shifts along lines of slope ~0.5. Quantities that could potentially be affected include $\delta^{17}O$, $\delta^{18}O$, $\delta^{26}Mg$, $\delta^{25}Mg$ and $^{27}Al/^{24}Mg$ ratios, while the $\Delta^{17}O$, radiogenic excess $\delta^{26}Mg^*$ and δ-values for calcium and titanium isotopes will be largely unaffected as they were internally corrected for additional mass fractionation after sample-standard bracketing. The bias in δ-values for oxygen and magnesium isotopes can arise in two ways. (1) Instrumental bias can affect unknowns individually due to differences in unknown chemistry (e.g., variable magnesium and titanium contents) or geometric effects (Kita et al., 2009), which could potentially account for different degrees of fractionation *within* the sample set, i.e., isotopically heavy and isotopically light compositions with respect to the CCAM line and some of the spread in the $\delta^{25}Mg$ vs. $\delta^{26}Mg$ diagram. (2) A constant bias can affect the data set as a whole and shift it towards heavy or light compositions due to differences in the chemical compositions of the standard and unknowns (e.g., higher FeO and REE contents in standard in the case of Madagascar hibonite, higher Si and Ca contents in the case of anorthite).

(1) First, we will exclude the possibility that variations in Murchison hibonite mineral chemistry are responsible for variations in the degree of fractionation *within* the unknown dataset. As there are resolvable mass-*independent* variations (spread in $\Delta^{17}O$) in addition to possible mass-dependent fractionation effects in oxygen isotopes, an evaluation of possible mass-dependent fractionation effects requires assumptions regarding the initial composition of the PLAC-like CAI precursors. Since the primary variation of the dataset is along a mass-independent line of slope ~1 similar to the CCAM line, the most reasonable choice is to assume that the precursors of PLAC-like CAIs initially fell along the CCAM line. Possible fractionation effects can then be compared by calculating the deviation of data from the CCAM line (in $\delta^{18}O$ in Fig. A2a). Using this notation, it becomes obvious that there is no relationship between mineral chemistry and the degree of fractionation in oxygen isotopes in the studied hibonites (Fig. A2a). In Fig. A2a, the Mg content is plotted, which can be used to assess the chemical variability in the studied grains as it is coupled with the abundances of $Ti^{4+}$and Al^{3+} ($Mg^{+2} + Ti^{+4} = 2\ Al^{+3}$), and no major variation in other elements was observed. The lack of a relationship between mineral chemistry and mass fractionation in oxygen isotopes (Fig. A2a) suggests that mineral chemistry did not influence instrumental fractionation for the studied hibonites. This is even the case for SHIB hibonites measured in the same session, which have a significantly larger range of magnesium and titanium contents than the PLAC-like CAIs but show minimal mass fractionation effects (Fig. A2a; Kööp et al., 2016). Similar to oxygen, there is no correlation between mineral chemistry and the degree of fractionation in magnesium isotopes (Fig. A2b). The data therefore suggest that variations in hibonite chemistry have no significant effect on instrumental fractionation of unknown measurements.

Similarly, geometric effects such as polishing relief or charging effects that could introduce additional fractionation for individual samples can be ruled out as topography was found to be minimal in the grain mounts (see Section 2.2). This is further substantiated by the consistently low values for the automatically adjusted deflector settings for all measurements, which can become elevated during automatic centering of the secondary beam in cases of uneven surfaces.

(2) While we can exclude that variations in unknown chemistry affect instrumental fractionation of individual hibonite analyses, the possibility remains that the dataset as a whole could be offset from true values in oxygen or magnesium because we had to use the FeO-rich Madagascar hibonite for fractionation correction. For oxygen, such a shift can likely be ruled out using the SHIB dataset, as

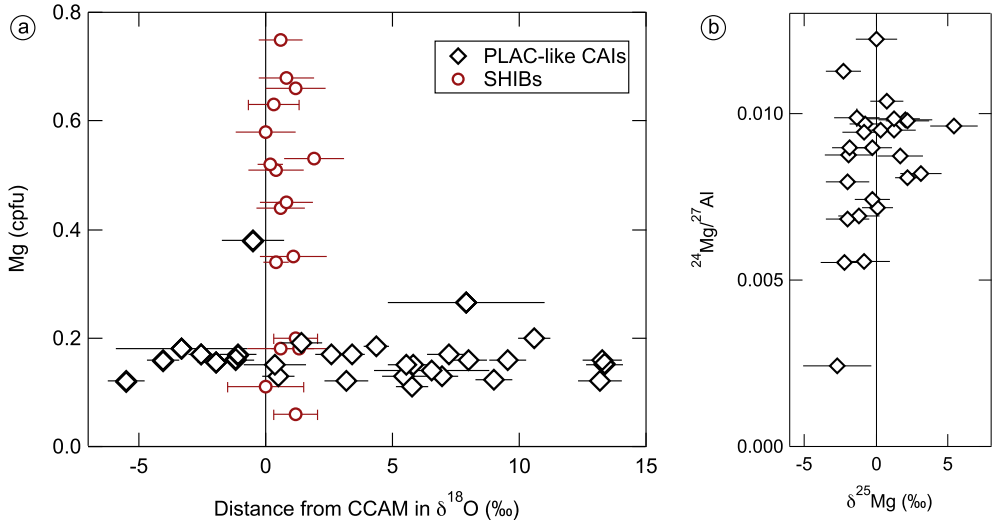

Fig. A2. Hibonite analyses show no relationship between mineral chemistry and the degree of mass fractionation in oxygen (a) and magnesium (b). Magnesium is a good proxy for the chemical variation of Murchison hibonites as titanium abundances mirror magnesium and are opposite to variations in aluminum (coupled substitution), and variations in other elements are minimal. The magnesium contents were obtained by EPMA (a) and by SIMS (b).

analyses of spinel and hibonite within the same SHIB typically agree within uncertainty and no consistent bias between hibonite and spinel analyses was found. Since spinel and hibonite SHIB data are on or only slightly offset from the CCAM line, using a Madagascar hibonite standard appears to introduce no or only a minimal a bias for oxygen isotopes.

Due to the lack of a suitable standard, we did not attempt to assess absolute δ^{25}Mg for the dataset. While the average δ^{25}Mg value in PLAC-like CAIs is indistinguishable from zero (0.0 ± 0.8‰), we used anorthite for normalization and thus expect that the dataset as a whole could be lighter or heavier by up to ~2‰ amu^{-1} due to the matrix effect. In contrast, the internal variations in PLAC-like CAIs of ~5‰ amu^{-1} in magnesium isotopes (Fig. 4) are likely intrinsic as chemical variation or topography in these samples is minimal (see above).

Similarly, the difference in unknown and standard composition can affect ^{27}Al/^{24}Mg ratios measured by SIMS. Based on SHIB data, we infer that the RSF bias is at the order of 5% at most, but due to the ^{26}Al-poor nature of the sample set, this small potential bias does not affect the conclusions of this study.

Finally, the possibility exists that some variations, in particular the mass-independent range in Δ^{17}O of ~11‰, are due to secondary processes or contamination. While exchange during aqueous alteration on the Murchison parent body could technically result in variations in oxygen isotopes (Clayton and Mayeda, 1984), the lack of isotopic variation in SHIB hibonites regardless of petrologic setting (fine-grained, coarse-grained, rimmed, located in the center or at edge of the inclusion as well as in direct proximity to alteration phases; Kööp et al., 2016) suggests that hibonite grains did not readily exchange with ^{16}O-poor liquids. Similarly, contamination can be excluded as the SHIBs and PLAC-like CAIs experienced the same preparation steps and because the small primary spot size of the Cs^+ primary beam during oxygen isotope analysis allowed us to efficiently avoid sampling of secondary phases, which was confirmed with the SEM after the analysis. We therefore conclude that the oxygen isotope data presented in Fig. 2 and Table 2 reflects the true composition of the studied CAIs. Deviations from the CCAM line are intrinsic and either due to isotope fractionation inherent from their formation processes or nucleosynthetic anomalies in oxygen isotopes.

A.3. Mass-fractionation correction for calcium and titanium isotopes

As outlined in Section 2.5.3, instrumental fractionation of calcium and titanium analyses was corrected by sample-standard bracketing and any potential intrinsic fractionation was corrected using a Rayleigh law. This is in contrast to previous studies, which corrected for both sources of mass-fractionation simultaneously by applying the exponential law (internal normalization). We decided to deviate from this convention for four main reasons. (1) It has been shown that evaporation of calcium and titanium from experimental melts results in isotopic fractionation that follows a Rayleigh law, not the exponential law (Zhang et al., 2014). (2) A number of standard analyses corrected with the exponential law yield δ-values that are resolved from 0‰ beyond calculated 2σ uncertainties (compare Table EA.2). This may indicate that fractionation of calcium and titanium isotopes inside the CAMECA IMS-1280 follows a law that is different from the exponential law. Nonzero standard δ^{50}Ti values are more often observed in ^{46}Ti/^{48}Ti normalization than in ^{49}Ti/^{47}Ti normalization (EA.2), possibly because of increased extrapolation using a law that does not accurately describe fractionation inside the instrument. If true, it is better to estimate the degree of instrumental fractionation for unknowns from bracketing standard measurements. (3) The range of δ^{50}Ti and δ^{48}Ca values is approximately 7‰ for standards corrected with the exponential law (compare EA.2). Given this spread, we believe that the 2σ uncertainties calculated for internally normalization data (on average ~2‰ for unknowns) underestimate the true uncertainty of our analyses. By sample-standard bracketing, we propagate the uncertainties associated with the bracketing standards, which yields larger uncertainties that probably reflect the true uncertainty of our measurements more accurately. (4) Finally, this data treatment is consistent with magnesium isotopic analyses, in which instrumental fractionation is corrected using sample-standard bracketing followed by correction of intrinsic fractionation using an appropriate law obtained from experiments (Davis et al., 2015).

Comparison of the two approaches: Sample-standard bracketing followed by correction with the Rayleigh law yields larger uncertainties (3–7‰ on both δ^{50}Ti and δ^{48}Ca) than internal correction with the exponential law (2–3‰ on both δ^{50}Ti and δ^{48}Ca). As noted above, this is because uncertainties of the bracketing standard analyses are propagated and is believed to reflect the true measurement uncertainties more accurately. As illustrated in Fig. A3 for titanium, the different approaches for fractionation correction have only small effects on calculated δ-values and the values overlap within 2σ uncertainties. This suggests that the newly obtained data can be compared with data from previous studies that used different mass-fractionation correction schemes.

A.4. Choice of normalization isotope pairs for titanium

Some of the studied PLAC-like CAIs have small anomalies in ^{49}Ti or ^{46}Ti when normalized to ^{46}Ti/^{48}Ti or ^{49}Ti/^{47}Ti, respectively. Previous studies concluded that the anomaly was in ^{49}Ti and thus normalized to ^{46}Ti/^{48}Ti (e.g., Fahey et al., 1985; Ireland, 1988, 1990; Liu et al., 2009), but the presence of small anomalies in ^{46}Ti in CV chondrite CAIs (Trinquier et al., 2009) casts doubts on whether ^{46}Ti should be used as a normalization isotope for PLAC-like CAIs. Anomalies in ^{46}Ti would produce artificial anomalies in ^{49}Ti of the same sign if the data are normalized to ^{46}Ti/^{48}Ti. The variation in PLAC-like CAIs could therefore be in ^{46}Ti rather than ^{49}Ti. For example, a +5‰ anomaly in ^{46}Ti would introduce artificial anomalies in ^{49}Ti and ^{50}Ti of +2.4‰ and +5‰ in ^{46}Ti/^{48}Ti normalization. Similarly, a +5‰ anomaly in ^{49}Ti would

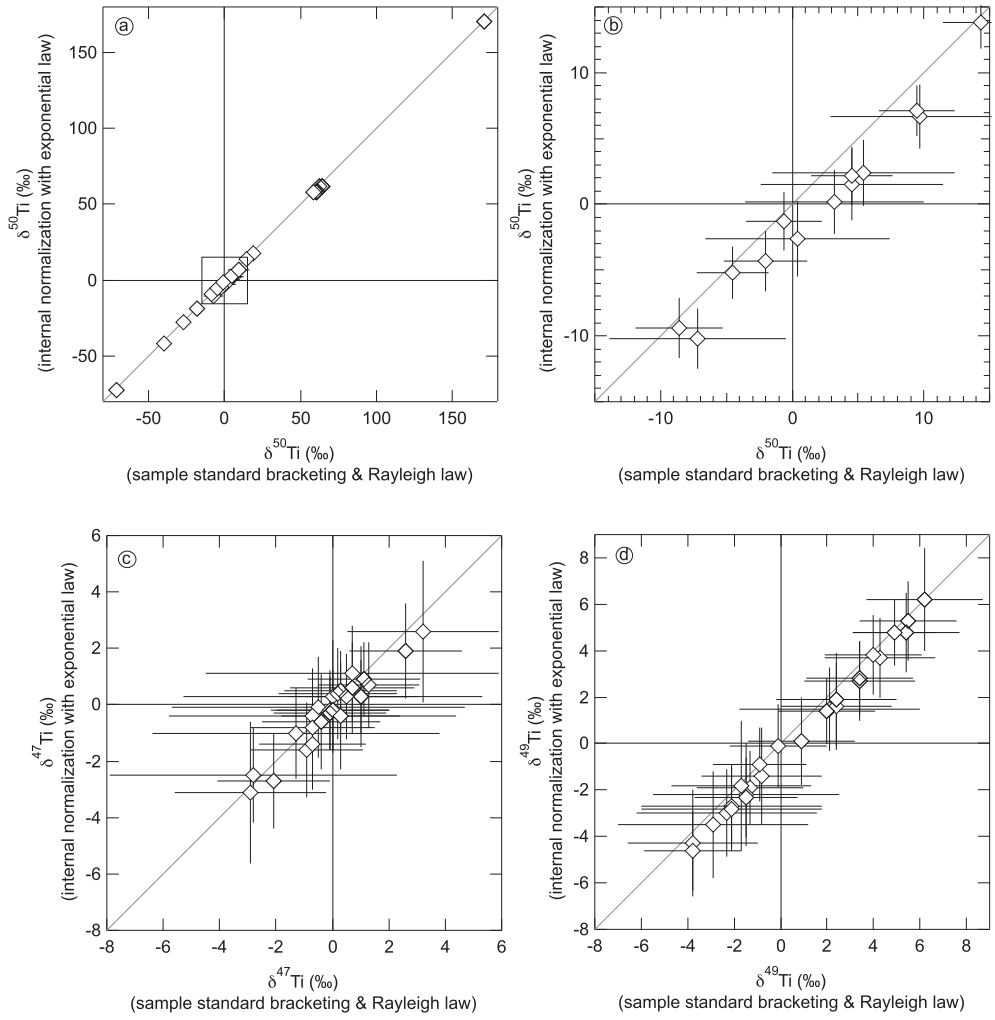

Fig. A3. Comparison of the titanium isotopic data processed with different approaches for mass-fractionation correction on δ^{50}Ti (a, b), δ^{47}Ti (c) and δ^{49}Ti (d). δ-Values obtained by internal correction of instrumental and intrinsic fractionation effects with the exponential law are plotted against *d*-values for which instrumental fractionation was corrected by sample-standard bracketing and intrinsic fractionation was corrected using a Rayleigh law. The area in the box in (a) is magnified in (b) to show the effects more clearly. All panels show that the differences in the magnitudes of calculated δ-values (deviations from a 1:1 line) are small compared to the calculated 2σ uncertainty of the data. The data is normalized to ^{46}Ti/^{48}Ti.

introduce artificial anomalies in ^{46}Ti and ^{50}Ti of +2.6‰ and −7‰ in ^{49}Ti/^{47}Ti normalization. Artificial variation in ^{46}Ti or ^{49}Ti is thus approximately half that of the normalizing isotope with the actual variation (i.e., ^{49}Ti or ^{46}Ti, respectively). Therefore, if the variation was only in one of the two isotopes, the range of artificial variation should be about half that of the actually variable isotope. Thus, comparison of the ranges of δ^{49}Ti and δ^{46}Ti values may be a way of identifying the better normalization pair. For our dataset, both δ^{49}Ti and δ^{46}Ti have a range of approximately 10‰, but while δ^{49}Ti values show a continuous distribution, the range of δ^{46}Ti values is mostly the result of two outliers, while the rest of the data show a range closer to 5‰. While the new dataset may thus hint at the variation being in ^{49}Ti for most studied grains, the situation seems different for the data recently compiled and renormalized by Steele and Boehnke (2015), which show a larger range in δ^{46}Ti than in δ^{49}Ti. PLAC-like CAIs thus appear to show small variations in both ^{46}Ti and ^{49}Ti and an ideal normalization pair may not exist. We emphasize again that the effect of the different normalization pairs on the magnitude of δ^{50}Ti values is small (Fig. 5) and has no consequence for the conclusions drawn in this study.

APPENDIX B. SUPPLEMENTARY DATA

Supplementary data associated with this article can be found, in the online version, at http://dx.doi.org/10.1016/j.gca.2016.05.014.

REFERENCES

Akram W., Schönbächler M., Sprung P. and Vogel N. (2013) Zirconium-hafnium isotope evidence for the decoupled synthe-

sis of light and heavy neutron-rich nuclei. *Astrophys. J.* **777**, #169 (12 pp).
Amari S., Lewis R. S. and Anders E. (1994) Interstellar grains in meteorites. I. Isolation of SiC, graphite, and diamond; size distributions of SiC and graphite. *Geochim. Cosmochim. Acta* **58**, 459–470.
Baertschi P. (1976) Absolute ^{18}O content of standard mean ocean water. *Earth Planet. Sci. Lett.* **31**, 341–344.
Bodénan J.-D., Starkey N. A., Russell S. S., Wright I. P. and Franchi I. A. (2014) An oxygen isotope study of Wark-Lovering rims on Type A CAIs in primitive carbonaceous chondrites. *Earth Planet. Sci. Lett.* **401**, 327–336.
Burkhardt C., Kleine T., Oberli F., Pack A., Bourdon B. and Wieler R. (2011) Molybdenum isotope anomalies in meteorites: constraints on solar nebula evolution and origin of the Earth. *Earth Planet. Sci. Lett.* **312**, 390–400.
Clayton R. N. (2002) Solar system: self-shielding in the solar nebula. *Nature* **415**, 860–861.
Clayton R. N. and Mayeda T. K. (1984) The oxygen isotope record in Murchison and other carbonaceous chondrites. *Earth Planet. Sci. Lett.* **67**, 151–161.
Clayton R. N., Grossman L. and Mayeda T. K. (1973) A component of primitive nuclear composition in carbonaceous meteorites. *Science* **182**, 485–488.
Clayton R. N., Onuma N., Grossman L. and Mayeda T. K. (1977) Distribution of the presolar component in Allende and other carbonaceous chondrites. *Earth Planet. Sci. Lett.* **34**, 209–224.
Clayton R. N., Hinton R. W. and Davis A. M. (1988) Isotopic variations in the rock-forming elements in meteorites. *Phil. Trans. R. Soc. Lond.* **A325**, 483–501.
Connelly J. N., Bizzarro M., Krot A. N., Nordlund Å., Wielandt D. and Ivanova M. A. (2012) The absolute chronology and thermal processing of solids in the solar protoplanetary disk. *Science* **338**, 651.
Dauphas N., Remusat L., Chen J. H., Roskosz M., Papanastassiou D. A., Stodolna J., Guan Y., Ma C. and Eiler J. M. (2010) Neutron-rich chromium isotope anomalies in supernova nanoparticles. *Astrophys. J.* **720**, 1577.
Dauphas N., Chen J. H., Zhang J., Papanastassiou D. A., Davis A. M. and Travaglio C. (2014) Calcium-48 isotopic anomalies in bulk chondrites and achondrites: evidence for a uniform isotopic reservoir in the inner protoplanetary disk. *Earth Planet. Sci. Lett.* **407**, 96–108.
Davis A. M., Richter F. M., Mendybaev R. A., Janney P. E., Wadhwa M. and McKeegan K. D. (2005) Isotopic mass fractionation laws and the initial solar system $^{26}Al/^{27}Al$ ratio. *Lunar Planet. Sci.* **36**, #2334.
Davis A. M., Richter F. M., Mendybaev R. A., Janney P. E., Wadhwa M. and McKeegan K. D. (2015) Isotopic mass fractionation laws for magnesium and their effects on ^{26}Al–^{26}Mg systematics in solar system materials. *Geochim. Cosmochim. Acta* **158**, 245–261.
Diehl R., Halloin H., Kretschmer K., Lichti G. G., Schönfelder V., Strong A. W., von Kienlin A., Wang W., Jean P., Knödlseder J., Roques J.-P., Weidenspointner G., Schanne S., Hartmann D. H., Winkler C. and Wunderer C. (2006) Radioactive ^{26}Al from massive stars in the Galaxy. *Nature* **439**, 45–47.
Fahey A. J. (1998) Measurements of dead time and characterization of ion counting systems for mass spectrometry. *Rev. Sci. Instrum.* **69**, 1282–1288.
Fahey A. J., Goswami J. N., McKeegan K. D. and Zinner E. (1985) Evidence for extreme ^{50}Ti enrichments in primitive meteorites. *Astrophys. J.* **296**, L17–L20.
Fahey A. J., Goswami J. N., McKeegan K. D. and Zinner E. (1987a) ^{16}O excess in Murchison and Murray hibonites: a case against a late supernove injection origin of isotopic anomalies in O, Mg, Ca, and Ti. *Astrophys. J.* **323**, L91–L95.
Fahey A. J., Goswami J. N., McKeegan K. D. and Zinner E. (1987b) ^{26}Al, ^{244}Pu, ^{50}Ti, REE, and trace element abundances in hibonite grains from CM and CV meteorites. *Geochim. Cosmochim. Acta* **51**, 329–350.
Gounelle M., Krot A. N., Nagashima K. and Kearley A. (2009) Extreme ^{16}O-enrichment in refractory inclusions from the Isheyevo meteorite: implication for oxygen isotope composition of the Sun. *Astrophys. J.* **698**, L18–L22.
Grossman L. (1972) Condensation in the primitive solar nebula. *Geochim. Cosmochim. Acta* **36**, 595–619.
Heck P. R., Ushikubo T., Schmitz B., Kita N. T., Spicuzza M. J. and Valley J. W. (2010) A single asteroidal source for extraterrestrial Ordovician chromite grains from Sweden and China: high-precision oxygen three-isotope SIMS analysis. *Geochim. Cosmochim. Acta* **74**, 497–509.
Hinton R. W., Davis A. M. and Scatena-Wachel D. E. (1987) Large negative ^{50}Ti anomalies in refractory inclusions from the Murchison carbonaceous chondrite: evidence for incomplete mixing of neutron-rich supernova ejecta into the solar system. *Astrophys. J.* **313**, 420–428.
Huss G. R., Meshik A. P., Smith J. B. and Hohenberg C. M. (2003) Presolar diamond, silicon carbide, and graphite in carbonaceous chondrites: implications for thermal processing in the solar nebula. *Geochim. Cosmochim. Acta* **67**, 4823–4848.
Ireland T. R. (1988) Correlated morphological, chemical, and isotopic characteristics of hibonites from the Murchison carbonaceous chondrite. *Geochim. Cosmochim. Acta* **52**, 2827–2839.
Ireland T. R. (1990) Presolar isotopic and chemical signatures in hibonite-bearing refractory inclusions from the Murchison carbonaceous chondrite. *Geochim. Cosmochim. Acta* **54**, 3219–3237.
Ireland T. R., Zinner E. K., Fahey A. J. and Esat T. M. (1992) Evidence for distillation in the formation of HAL and related hibonite inclusions. *Geochim. Cosmochim. Acta* **56**, 2503–2520.
Jacobsen B., Yin Q., Moynier F., Amelin Y., Krot A. N., Nagashima K., Hutcheon I. D. and Palme H. (2008) ^{26}Al–^{26}Mg and ^{207}Pb–^{206}Pb systematics of Allende CAIs: canonical solar initial $^{26}Al/^{27}Al$ ratio reinstated. *Earth Planet. Sci. Lett.* **272**, 353–364.
Kawasaki N., Sakamoto N. and Yurimoto H. (2012) Oxygen isotopic and chemical zoning of melilite crystals in a Type A Ca–Al-rich inclusion of Efremovka CV3 chondrite. *Meteorit. Planet. Sci.* **47**, 2084–2093.
Kita N. T., Ushikubo T., Fu B. and Valley J. W. (2009) High precision SIMS oxygen isotope analysis and the effect of sample topography. *Chem. Geol.* **264**, 43–57.
Kita N. T., Nagahara H., Tachibana S., Tomomura S., Spicuzza M. J., Fournelle J. H. and Valley J. W. (2010) High precision SIMS oxygen three isotope study of chondrules in LL3 chondrites: role of ambient gas during chondrule formation. *Geochim. Cosmochim. Acta* **74**, 6610–6635.
Kita N. T., Ushikubo T., Knight K. B., Mendybaev R. A., Davis A. M., Richter F. M. and Fournelle J. H. (2012) Internal ^{26}Al–^{26}Mg isotope systematics of a Type B CAI: remelting of refractory precursor solids. *Geochim. Cosmochim. Acta* **86**, 37–51.
Kobayashi S., Imai H. and Yurimoto H. (2003) An extreme ^{16}O-rich chondrule from Acfer 214 CH chondrite. *Lunar Planet. Sci.* **34**, #1536.
Kööp L., Davis A. M., Heck P. R., Kita N. T., Krot A. N., Mane P., Nagashima K., Nakashima D., Park C., Tenner T. J. and Wadhwa M. (2015) Multiple generations of fractionated

hibonite-rich CAIs sampled the solar nebula at different degrees of isotopic heterogeneity. *Lunar Planet. Sci* **46**, #2750.

Kööp L., Nakashima D., Heck P. R., Kita N. T., Tenner T. J., Krot A. N., Nagashima K., Park C. and Davis A. M. (2016) New constraints on the relationship between ^{26}Al and oxygen, calcium, and titanium isotopic variation in the early Solar System from a multielement isotopic study of spinel-hibonite inclusions. *Geochim. Cosmochim. Acta* **184**, 151–172.

Krot A. N., Nagashima K., Bizzarro M., Huss G. R., Davis A. M., Meyer B. S. and Ulyanov A. A. (2008) Multiple generations of refractory inclusions in the metal-rich carbonaceous chondrites Acfer 182/214 and Isheyevo. *Astrophys. J.* **672**, 713–721.

Krot A. N., Amelin Y., Bland P., Ciesla F. J., Connelly J., Davis A. M., Huss G. R., Hutcheon I. D., Makide K., Nagashima K., Nyquist L. E., Russell S. S., Scott E. R. D., Thrane K., Yurimoto H. and Yin Q.-Z. (2009) Origin and chronology of chondritic components: a review. *Geochim. Cosmochim. Acta* **73**, 4963–4997.

Krot A. N., Nagashima K., Ciesla F. J., Meyer B. S., Hutcheon I. D., Davis A. M., Huss G. R. and Scott E. R. D. (2010) Oxygen isotopic composition of the Sun and mean oxygen isotopic composition of the protosolar silicate dust: evidence from refractory inclusions. *Astrophys. J.* **713**, 1159–1166.

Krot A. N., Nagashima K., Wasserburg G. J., Huss G. R., Papanastassiou D., Davis A. M., Hutcheon I. D. and Bizzarro M. (2014) Calcium–aluminum-rich inclusions with fractionation and unknown nuclear effects (FUN CAIs): I. Mineralogy, petrology, and oxygen isotopic compositions. *Geochim. Cosmochim. Acta* **145**, 206–247.

Krot A. N., Nagashima K., van Kooten E. M. M. E. and Bizzarro M. (2015) Refractory inclusions recycled during formation of porphyritic chondrules from CH carbonaceous chondrites. *Lunar Planet. Sci* **46**, #1596.

Lee J.-E., Bergin E. A. and Lyons J. R. (2008) Oxygen isotope anomalies of the Sun and the original environment of the solar system. *Meteorit. Planet. Sci.* **43**, 1351–1362.

Liu M.-C., McKeegan K. D., Goswami J. N., Marhas K. K., Sahijpal S., Ireland T. R. and Davis A. M. (2009) Isotopic records in CM hibonites: implications for timescales of mixing of isotope reservoirs in the solar nebula. *Geochim. Cosmochim. Acta* **73**, 5051–5079.

Liu M.-C., Chaussidon M., Göpel C. and Lee T. (2012) A heterogeneous solar nebula as sampled by CM hibonite grains. *Earth Planet. Sci. Lett.* **327**, 75–83.

Lodders K. (2003) Solar system abundances and condensation temperatures of the elements. *Astrophys. J.* **591**, 1220–1247.

Lyons J. R. and Young E. D. (2005) CO self-shielding as the origin of oxygen isotope anomalies in the early solar nebula. *Nature* **435**, 317–320.

MacPherson G. J., Nagashima K., Bullock E. S. and Krot A. N. (2008) Mass-dependent oxygen isotopic fractionation in non-FUN forsterite-bearing Type B CAIs. *Lunar Planet. Sci.* **39**, #2039.

MacPherson G. J., Kita N. T., Ushikubo T., Bullock E. S. and Davis A. M. (2012) Well-resolved variations in the formation ages for Ca–Al-rich inclusions in the early solar system. *Earth Planet. Sci. Lett.* **331**, 43–54.

Makide K., Nagashima K., Krot A. N., Huss G. R., Hutcheon I. D. and Bischoff A. (2009) Oxygen- and magnesium-isotope compositions of calcium–aluminum-rich inclusions from CR2 carbonaceous chondrites. *Geochim. Cosmochim. Acta* **73**, 5018–5050.

McKeegan K. D., Kallio A. P. A., Heber V. S., Jarzebinski G., Mao P. H., Coath C. D., Kunihiro T., Wiens R. C., Nordholt J. E., Moses R. W., Reisenfeld D. B., Jurewicz A. J. G. and Burnett (2011) The oxygen isotopic composition of the Sun inferred from captured solar wind. *Science* **332**, 1528–1532.

Mendybaev R. A., Richter F. M., Georg R. B., Janney P. E., Spicuzza M. J., Davis A. M. and Valley J. W. (2013) Experimental evaporation of Mg- and Si-rich melts: implications for the origin and evolution of FUN CAIs. *Geochim. Cosmochim. Acta* **123**, 368–384.

Nakashima D., Ushikubo T., Gowda R. N., Kita N. T., Valley J. W. and Nagao K. (2011) Ion microprobe analyses of oxygen three-isotope ratios of chondrules from the Sayh al Uhaymir 290 CH chondrite using a multiple-hole disk. *Meteorit. Planet. Sci.* **46**, 857–874.

Nittler L. R., Alexander C. M. O., Gallino R., Hoppe P., Nguyen A. N., Stadermann F. J. and Zinner E. K. (2008) Aluminum-, calcium- and titanium-rich oxide stardust in ordinary chondrite meteorites. *Astrophys. J.* **682**, 1450–1478.

Nozawa T., Maeda K., Kozasa T., Tanaka M., Nomoto K. and Umeda H. (2011) Formation of dust in the ejecta of Type Ia supernovae. *Astrophys. J.* **736**, 45.

Park C., Wakaki S., Sakamoto N., Kobayashi S. and Yurimoto H. (2012) Oxygen isotopic composition of the solar nebula gas inferred from high-precision isotope imaging of melilite crystals in an Allende CAI. *Meteorit. Planet. Sci.* **47**, 2070–2083.

Park C., Nagashima K., Hutcheon I. D., Wasserburg G. J., Papanastassiou D. A., Davis A. M., Huss G. R. and Krot A. N. (2013) Heterogeneity of Mg isotopes and variable ^{26}Al/^{27}Al ratio in FUN CAIs. *Meteor. Planet. Sci. Suppl.* **76**, #5085.

Park C., Nagashima K., Wasserburg G. J., Papanastassiou D. A., Hutcheon I. D., Davis A. M., Huss G. R., Bizzarro M. and Krot A. N. (2014) Calcium and titanium isotopic compositions of FUN CAIs: implications for their origin. *Lunar Planet. Sci* **45**, #2656.

Rauscher T., Heger A., Hoffman R. D. and Woosley S. E. (2002) Nucleosynthesis in massive stars with improved nuclear and stellar physics. *Astrophys. J.* **576**, 323–348.

Richter F. M., Davis A. M., Ebel D. S. and Hashimoto A. (2002) Elemental and isotopic fractionation of Type B calcium-, aluminum-rich inclusions: experiments, theoretical considerations, and constraints on their thermal evolution. *Geochim. Cosmochim. Acta* **66**, 521–540.

Sahijpal S. and Goswami J. N. (1998) Refractory phases in primitive meteorites devoid of ^{26}Al and ^{41}Ca: representative samples of first solar system solids? *Astrophys. J.* **509**, L137–L140.

Sahijpal S., Goswami J. N. and Davis A. M. (2000) K, Mg, Ti and Ca isotopic compositions and refractory trace element abundances in hibonites from CM and CV meteorites: implications for early solar system processes. *Geochim. Cosmochim. Acta* **64**, 1989–2005.

Schönbächler M., Lee D.-C., Rehkämper M., Halliday A. N., Fehr M. A., Hattendorf B. and Günther D. (2003) Zirconium isotope evidence for incomplete admixing of r-process components in the solar nebula. *Earth Planet. Sci. Lett.* **216**, 467–481.

Simon J. I., Hutcheon I. D., Simon S. B., Matzel J. E. P., Ramon E. C., Weber P. K., Grossman L. and DePaolo D. J. (2011) Oxygen isotope variations at the margin of a CAI records circulation within the solar nebula. *Science* **331**, 1175–1178.

Steele R. C. J. and Boehnke P. (2015) Titanium isotope source relations and the extent of mixing in the proto-solar nebula examined by independent component analysis. *Astrophys. J.* **802**, 80–93.

Thiemens M. H. (2006) History and applications of mass-independent isotope effects. *Ann. Rev. Earth Planet. Sci.* **34**, 217–262.

Trinquier A., Elliott T., Ulfbeck D., Coath C., Krot A. N. and Bizzarro M. (2009) Origin of nucleosynthetic isotope heterogeneity in the solar protoplanetary disk. *Science* **324**, 374–376.

Ushikubo T., Kimura M., Kita N. T. and Valley J. W. (2011) Primordial oxygen isotope reservoirs of the solar nebula recorded in chondrules from Acfer 094 carbonaceous chondrite. *Lunar Planet. Sci.* **42**, #1183.

Ushikubo T., Kimura M., Kita N. T. and Valley J. W. (2012) Primordial oxygen isotope reservoirs of the solar nebula recorded in chondrules in Acfer 094 carbonaceous chondrite. *Geochim. Cosmochim. Acta* **90**, 242–264.

Ushikubo T., Nakashima D., Kimura M., Tenner T. J. and Kita N. T. (2013) Contemporaneous formation of chondrules in distinct oxygen isotope reservoirs. *Geochim. Cosmochim. Acta* **109**, 280–295.

Wasserburg G., Lee T. and Papanastassiou D. (1977) Correlated O and Mg isotopic anomalies in Allende inclusions: II. Magnesium. *Geophys. Res. Lett.* **4**, 299–302.

Wood J. A. (1998) Meteoritic evidence for the infall of large interstellar dust aggregates during the formation of the solar system. *Astrophys. J.* **503**, L101–L104.

Yang L., Ciesla F. J., Lyons J. R., Lee J.-E. and Bergin E. A. (2011) Oxygen isotope anomalies in the solar nebula inherited from the proto-solar cloud. *Lunar Planet. Sci.* **42**, #1602.

Young E. D. and Russell S. S. (1998) Oxygen reservoirs in the early solar nebula inferred from an Allende CAI. *Science* **282**, 452–455.

Yurimoto H. and Kuramoto K. (2004) Molecular cloud origin for the oxygen isotope heterogeneity in the solar system. *Science* **305**, 1763–1766.

Zinner E. K., Fahey A. J., McKeegan K. D., Goswami J. N. and Ireland T. R. (1986) Large ^{48}Ca anomalies are associated with ^{50}Ti anomalies in Murchison and Murray hibonites. *Astrophys. J.* **311**, L103–L107.

Zinner E. K., Fahey A. J., McKeegan K. D. and Goswami J. N. (1987) Isotopic structures in Murchison hibonites: O, Ca, and Ti. *Meteoritics* **22**, 542–543.

Zhang J., Davis A. M. and Dauphas N. (2012) Titanium isotopic compositions in calcium–aluminum-rich inclusions. *Meteor. Planet. Sci. Suppl.* **47**, #5286.

Zhang J., Huang S., Davis A. M., Dauphas N., Hashimoto A. and Jacobsen S. B. (2014) Calcium and titanium isotopic fractionations during evaporation. *Geochim. Cosmochim. Acta* **140**, 365–380.

Associate editor: Munir Humayun